Engineering xxx (xxxx) xxx

Contents lists available at ScienceDirect

Engineering

journal homepage: www.elsevier.com/locate/eng

Research
Civil Engineering—Article

Intelligent Forming of Large-Span Arch Bridges: Methodology and Engineering Applications

Jianting Zhou [a,b], Yanliang Du [c], Yin Zhou [a,b,*], Jinyu Zhu [a,b]

[a] State Key Laboratory of Mountain Bridge and Tunnel Engineering, Chongqing Jiaotong University, Chongqing 400074, China
[b] School of Civil Engineering, Chongqing Jiaotong University, Chongqing 400074, China
[c] College of Civil and Transportation Engineering, Shenzhen University, Shenzhen 518060, China

ARTICLE INFO

Article history:
Received 2 December 2024
Revised 14 September 2025
Accepted 29 October 2025
Available online xxxx

Keywords:
Large-span arch bridge
Intelligent construction
Arch-forming calculation
Manufacturing control
Installation technology

ABSTRACT

Arch bridges are well-suited to mountainous regions because their force characteristics align with local site conditions. However, construction in such areas faces challenges including large temperature differentials, complex canyon wind fields, and rugged terrain. Arch-forming also entails extensive work at height, high construction risk, and difficulties in achieving precise alignment after forming. To overcome these issues, this study presents an intelligent arch-forming method for large-span arch bridges. First, an optimization model for the entire arch-forming process is established to compute cable forces that meet objectives during construction. Second, a digital preassembly-based manufacturing control scheme is developed, allowing high-precision virtual assembly of arch rib segments in a digital environment. Finally, an automatic installation attitude adjustment strategy is proposed, based on restoring the structure to its designed shape, enabling high-precision, automated adjustment of the three-dimensional installation attitude of arch rib segments. The proposed method has been successfully applied to the Deyu Expressway Wujiang Bridge (with a main span of 504 m) located in Guizhou Province, China, demonstrating its reliability and practicality. This approach offers guidance for low-labor, resource-efficient, rapid, and automated construction of large-span arch bridges.

1. Introduction

In recent years, an increasing number of transportation infrastructures have been constructed in mountainous regions [1,2]. Arch bridges, known for their high stiffness, strong disaster resistance, and excellent durability, are particularly suitable for such terrains because their force characteristics naturally align with the topographical features of mountainous areas [3]. The span of arch bridges has expanded rapidly, with a 600 m-level bridge completed and operational in 2024 [4]. Recognizing the development potential of large-span arch bridges, several scholars have proposed concepts for constructing 700 m-level structures [5,6]. However, compared with plains, mountainous regions present challenges such as rugged terrain, constrained construction sites, and complex natural conditions. These factors necessitate substantial labor and equipment, while large temperature variations and canyon wind fields cause significant fluctuations in the alignment and stress of arch ribs during construction. Traditional measurement and control methods are insufficient to achieve the required high-precision closure, and the elevated installation of arch ribs increases safety risks. To address these challenges, intelligent construction methods for large-span arch bridges have emerged as a key research focus, primarily involving arch-forming calculation, manufacturing control, and installation technology.

The cable-stayed fastening–hanging cantilever assembly method is the primary construction technique for large-span arch bridges. This approach involves temporarily erecting a suspension cable–inclined cable composite system to support the arch ribs during construction, which is then dismantled after the arch is formed to achieve the final bridge structure [1]. However, this method complicates the arch-forming calculation process. Due to the multiple construction stages, the force system changes frequently, making it challenging to control the final bridge alignment. Additionally, the method introduces numerous variables into the arch-forming optimization process, which must account for multiple objectives—such as alignment accuracy, tower

* Corresponding author at: State Key Laboratory of Mountain Bridge and Tunnel Engineering, Chongqing Jiaotong University, Chongqing 400074, China.
E-mail address: zhouyin@cqjtu.edu.cn (Y. Zhou).

https://doi.org/10.1016/j.eng.2025.10.022

Please cite this article as: J. Zhou, Y. Du, Y. Zhou et al., Intelligent Forming of Large-Span Arch Bridges: Methodology and Engineering Applications, Engineering, https://doi.org/10.1016/j.eng.2025.10.022

deviation, and cable force safety—across all construction stages. These factors significantly increase the complexity of the optimization. Therefore, developing intelligent optimization methods for arch-forming calculations in large-span arch bridges has become an important research direction.

During the manufacturing of large arch rib segments, large-scale physical assembly is typically performed in factories or on-site [7] to ensure precise matching between the main arch ribs and connecting components (e.g., flanges), thereby meeting alignment requirements after segmental connections. However, under the spatial and logistical constraints of mountainous sites, full pre-assembly of all segments is often impractical. This limitation can lead to cumulative alignment deviations in the assembled arch ribs. Furthermore, physical assembly requires substantial space, labor, and large equipment, which considerably increases both cost and construction time [8]. Therefore, a digital, high-precision assembly control method is urgently needed to replace traditional physical preassembly.

During the installation of arch rib segments, traditional methods employ total stations or similar single-point measurement instruments to record the coordinates of a few marked points on the arch ribs. The adjustment process is then performed multiple times through manual control of mechanical equipment [9,10]. These traditional methods cannot accurately capture the three-dimensional (3D) installation alignment of the arch ribs, necessitating frequent adjustments during installation to ensure the correct overall alignment of the main arch. Moreover, repeated manual adjustments using cable cranes are highly inefficient and pose safety risks. Thus, an intelligent and efficient installation control method for arch bridges is needed.

In summary, achieving low-labor, resource-efficient, rapid, and automated construction of large-span arch bridges in complex environments remains a major engineering challenge. To address this issue, this study proposes an intelligent arch-forming method for large-span arch bridges that enables precise and automated control of the calculation, manufacturing, and installation processes. This method enhances alignment accuracy and improves overall construction efficiency. The proposed approach was validated during the construction of the Deyu Expressway Wujiang Bridge (main span 504 m), demonstrating its reliability in practical engineering applications. The primary contributions of this study are as follows:

(1) An optimization model for the entire arch-forming process is proposed, linking the mechanical states before and after cable removal. The model defines constraint equations and an objective function to determine one-time cable tensioning forces that satisfy tower deviation limits, cable force safety, and alignment targets throughout construction.

(2) A manufacturing control scheme based on digital preassembly of the arch ribs is developed, incorporating a dual-weight point cloud to building information model (BIM) alignment algorithm. This enables high-precision virtual preassembly of arch rib segments in the digital environment.

(3) An automatic installation attitude adjustment strategy for arch ribs based on original shape restoration is proposed, including an algorithm to compute and adjust the 3D attitude of arch rib segments under load. This allows precise one-time installation of arch rib segments.

The remainder of this paper is organized as follows: Section 2 reviews related work. Section 3 introduces the proposed intelligent control methods for large-span arch bridges. Section 4 validates the accuracy, reliability, and practicality of the methods using construction results from the Deyu Expressway Wujiang Bridge. Finally, Section 5 presents the conclusions.

2. Related works

The arch formation process of a long-span arch bridge consists of three key stages: arch-forming calculation, manufacturing control, and installation adjustment. The arch-forming calculation determines both the manufacturing alignment of arch rib segments and a rational cable force scheme for the installation process. High-precision manufacturing of arch ribs ensures that their geometry closely matches the target alignment, thereby minimizing the number of adjustments required during installation at high altitudes. During installation, further adjustments are made to correct any residual errors in the arch rib alignment, ensuring that the final formed arch conforms to the design target. This section presents the theoretical basis of arch-forming calculations and reviews the current research on manufacturing control and installation adjustment techniques.

In arch-forming calculations, cable forces play a crucial role in controlling the alignment of arch ribs, tower deviations during construction, and internal forces within the arch bridge. Traditional methods for determining cable forces include the zero-moment method, zero-displacement method, fixed-length cable method, and optimization method. The zero-moment method [11] focuses on minimizing bending moments in the main arch but is insufficient for controlling post-construction displacements. The zero-displacement method [12], which targets the displacement of arch ribs, often results in compressive cable forces that lack physical feasibility. The fixed-length cable method [13] improves construction safety and efficiency by enabling one-time cable tensioning, though calculating the appropriate unstressed cable lengths to satisfy multiple constraints remains challenging.

Optimization-based methods have become a primary research focus. Li et al. [14] optimized cable force determination by combining influence matrices and linear programming to achieve one-time tensioning and accurate arch rib alignment. Huo et al. [15] applied the vector iteration method to calculate cable forces during the construction of multirib butterfly arch bridges. Qin et al. [16] employed influence matrix principles and optimization theory to determine initial cable forces during construction. Zhou et al. [17] incorporated temperature variation effects on arch rib displacements, deriving relationships among temperature changes, arch rib elevations, and cable angles to improve computational efficiency. Zhang et al. [18] derived load integrals for uniform temperature changes and simplified the structural analysis of arch bridges into equivalent straight beam systems, verifying the reliability of the method with illustrative examples. Moreover, recent studies [19,20] have utilized machine learning and finite element collaborative simulations to optimize cable forces during arch bridge construction. However, most existing methods optimize only specific construction stages and fail to simultaneously address all stages of the process. Furthermore, arch-forming calculations must balance multiple objectives—such as tower deviation, cable force safety, and post-forming alignment—which greatly increases the complexity of achieving integrated optimization.

In terms of manufacturing control, the primary method used for large-span arch bridges is the "N + 1" segment physical trial assembly. However, this approach requires multiple rounds of physical assembly, consuming substantial manpower, space, and mechanical resources. Even after repeated assemblies, the overall alignment of the fully assembled arch ribs cannot be fully verified. To overcome these limitations, researchers have explored virtual trial assembly (VTA) techniques to digitally simulate the physical assembly process. In the field of architecture, Case et al. [21] proposed a steel structure VTA method based on generalized Procrustes analysis, which was applied to the Chernobyl Nuclear Reactor Project to enhance bolt detection efficiency. Maset et al.

[22] introduced an affine extended orthogonal Procrustes analysis (EOPA) method to eliminate component deviations through single-spacer plate insertion, which was successfully applied to the dog-bone component assembly of New York's Vessel structure. Jiang et al. [8] developed a VTA method based on EOPA to quantify cumulative deviations between precast components and their nominal specifications, demonstrating its effectiveness in a two-story prefabricated frame. In bridge engineering, Tamai et al. [23] proposed the computerized assembly test system for use in the VTA of a steel bridge in Japan. Wang et al. [24] and Cheng et al. [7] applied the VTA method in suspension bridges to verify its feasibility and improve manufacturing precision. However, these methods do not actively control alignment precision during segment fabrication.

Regarding bridge installation technology, recent research has focused on intelligent recognition of construction states using computer vision and laser scanning techniques. Computer vision is widely applied in progress monitoring and quality control [25]. Jin et al. [26] integrated computer vision with deep learning to enhance camera robustness for pose detection. Tang et al. [27] used monocular vision to monitor the cable lifting structure during the construction of the Xininghe Bridge, a critical structure on the Chengdu–Guiyang high-speed railway in Xingwen County, Sichuan Province, achieving a single-axis displacement measurement error of less than 2 mm. Sensor data have also been employed to evaluate the effects of external loads on bridge performance [28,29]. For example, Huang et al. [30] proposed a sparse Bayesian temperature–displacement relationship (TDR) model to monitor and predict bearing displacement responses induced by temperature effects in arch bridges. Terrestrial laser scanners (TLSs) can efficiently collect large volumes of accurate 3D geometric data and have been applied in structural monitoring [31], reverse modeling [32], and dimensional inspection [33] of bridges. Kim et al. [34] combined TLS with BIM technology for dimensional inspection and quality management of precast concrete bridge components. Xu et al. [35] proposed a 3D laser scanning-based attitude measurement technique to guide the installation of precast bridge piers. These technologies have significantly enhanced state perception efficiency during bridge construction. However, research on intelligent perception specifically for the installation of long-span arch bridge segments remains limited. Current studies mainly address accurate recognition of bridge states, but further research is needed on precise adjustment methods following the acquisition of installation attitude data.

3. Methodology

Fig. 1 presents the proposed framework of the intelligent arch-forming method for long-span arch bridges, which comprises three main components: optimized arch-forming calculation, high-precision manufacturing of arch ribs, and rapid installation of arch rib segments. First, an optimization calculation model is developed for the entire arch-forming process. This model establishes the mechanical connections, constraint equations, and objective functions, providing both the optimal alignment for arch rib manufacturing and the optimal cable force scheme for installation control, as detailed in Section 3.1. Second, a manufacturing control scheme based on digital preassembly of arch ribs is proposed to achieve high-precision fabrication. In this approach, a high-fidelity model of each independently manufactured arch rib segment is generated using terrestrial laser scanning. The arch segments are then virtually preassembled in a digital environment to determine the optimal alignment of segment joints, which guides the precise machining of the joint nodes, as described in Section 3.2. Finally, an automatic installation attitude adjustment strategy based on original-shape restoration is introduced to minimize manual intervention and reduce construction risk during high-altitude segment installation. This method utilizes the high-fidelity 3D model obtained during the manufacturing phase as the initial alignment reference. It accounts for deformations in the main arch caused by environmental influences and cable forces to compute the 3D target alignment for arch segment installation. An automatic fine-tuning algorithm is subsequently applied to the attitude adjustment systems of both segment types, as explained in Section 3.3.

3.1. Optimization calculation for arch bridge formation

The key difference between the cable-stayed fastening–hanging system used in arch bridge construction and a conventional cable-stayed bridge lies in the target state being controlled, which is fundamentally distinct for the two systems. In a cable-stayed bridge, after cable-force adjustment, the stay cables remain as permanent structural components and are not removed. In contrast, in the fastening–hanging system, the cables are temporary, and the structural states before and after cable removal differ significantly, making cross-system construction control particularly challenging. To address the closure problem in cross-system arch bridge construction, this study establishes mechanical state connection equations that link the construction process with the final alignment after arch formation, thereby overcoming the limitations of methods such as that of Qin et al. [36], which control the final alignment of cable-stayed bridges through cable-force adjustment.

For cable-force control in the cable-stayed fastening–hanging system used in arch bridge construction, conventional approaches include the zero-moment method, zero-displacement method, fixed-length cable method, and optimization method. These methods treat the states before and after cable removal as separate. They focus primarily on the pre-removal phase—specifically, the

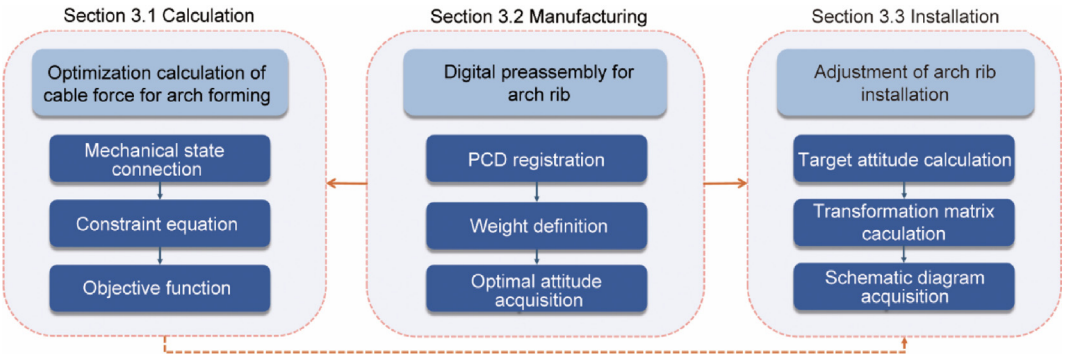

Fig. 1. Flowchart of the proposed method.

alignment and control—with the goal of achieving a "process optimal, result controllable" outcome. However, they cannot accurately quantify how variations in cable forces during construction affect the final arch alignment, nor can they control the final alignment through pre-removal cable adjustments. In contrast, the proposed arch-forming optimization method based on mechanical state connection equations explicitly defines and quantifies the influence of pre-removal cable forces on the final formed arch alignment.

The framework of this method is illustrated in Fig. 2. The study establishes a linkage between the mechanical state of cable forces during construction and the alignment of the arch after formation, achieving whole-process optimization of arch rib alignment throughout construction and after completion. Constraint equations are then formulated to account for alignment deviation after arch formation, tower alignment deviation during construction, the effect of initial cable tension, and cable force safety. An objective function is defined to minimize the coefficient of variation of cable forces across the construction process, using cable forces as variables. Finally, multiobjective optimization is performed based on the state connection relationships, constraint equations, and objective function [37]. This results in a comprehensive optimization calculation method for arch bridge construction that ensures optimal cable forces, controllable tower deviations, and minimal alignment deviations after arch formation. The framework of this method is shown in Fig. 2, and its derivation and implementation process are described in detail in the following sections.

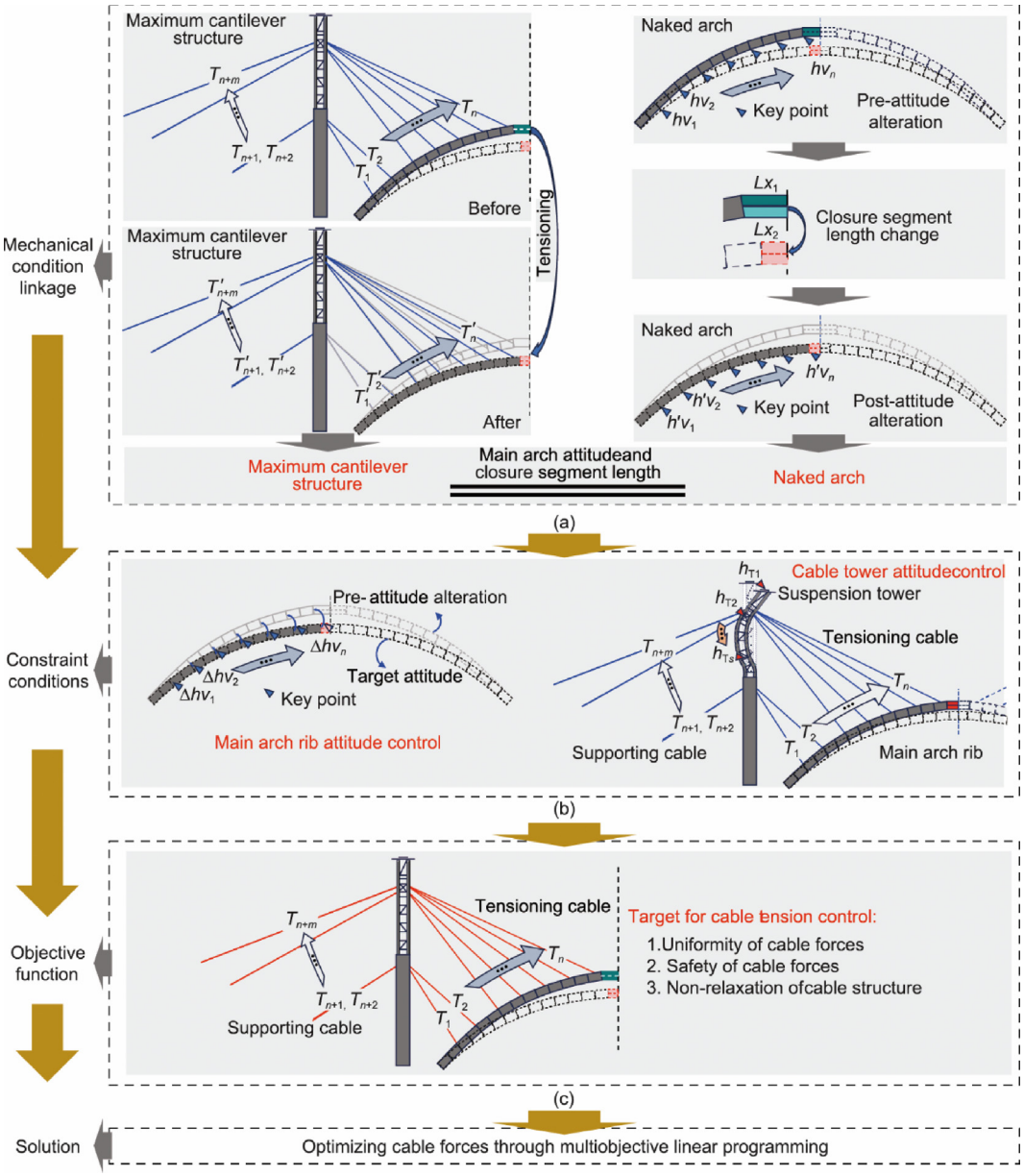

Fig. 2. Framework of the proposed optimization method. (a) Mechanical state connection; (b) constraint conditions; (c) objective function. $T_1, T_2, T_3, \ldots, T_n, T_{n+1}, T_{n+2}, \ldots, T_{n+m}$: cable force before adjustment; $T'_1, T'_2, T'_3, \ldots, T'_{n+1}, T'_{n+2}, \ldots, T'_{n+m}$: adjusted cable force; $hv_1, hv_2, \ldots, hv_n$: elevations of the control points for the main arch closure before cable adjustment; $hv'_1, hv'_2, \ldots, hv'_n$: elevations of the control points for the main arch closure after cable adjustment; $h_{T1}, h_{T2}, \ldots, h_{Ts}$: deviations of the control points on the tower, where s represents the serial number of each control point on the tower; $\Delta hv_1, \Delta hv_2, \ldots, \Delta hv_n$: alignment deviation aft er arch formation; Lx_1, Lx_2: unit variations in the upper and lower segments of the closure segment, respectively; n is the total number of cables and main arch control points; m represents the total number of cables.

3.1.1. Mechanical state connection

As shown in Fig. 2(a), the displacement errors generated at various measurement points of the central arch rib after changes in stress-free parameters can be expressed by Eq. (1). This equation is derived by considering the bare arch structure and integrating the influence matrix method to calculate and adjust the structural displacement and internal forces [38].

$$\boldsymbol{C}_1\begin{Bmatrix} Lx_1 \\ Lx_2 \end{Bmatrix} = \begin{Bmatrix} hv_1 \\ hv_2 \\ \vdots \\ hv_n \end{Bmatrix}; \begin{Bmatrix} hv_1 \\ hv_2 \\ \vdots \\ hv_n \end{Bmatrix} = \begin{Bmatrix} hg_1 \\ hg_2 \\ \vdots \\ hg_n \end{Bmatrix} - \begin{Bmatrix} hvo_1 \\ hvo_2 \\ \vdots \\ hvo_n \end{Bmatrix} \tag{1}$$

where $\boldsymbol{C}_1$ is the influence matrix that characterizes the deformation deviation of the arch rib alignment after cable removal when the stress-free states of the upper and lower closure segments change by Lx_1 and Lx_2. During the model calculation process, the influence matrix $\boldsymbol{C}_1$ is obtained by applying equivalent strain increments to the upper and lower units of the closure segment. hg_n denotes the displacement at measurement point n of the central arch rib under its self-weight when the bare arch structure is directly formed (without considering the construction process), hvo_n represents the displacement at the same point after a change in the stress-free parameters of the closure segment.

Fig. 2(a) depicts the maximum cantilever structure. The influence matrix of the cable force on the deformation of the cantilever structure is defined in Eq. (2):

$$\boldsymbol{C}_2\boldsymbol{T}^{\mathrm{T}} = \begin{Bmatrix} Lx_1 \\ Lx_2 \end{Bmatrix} - \begin{Bmatrix} Lxg_1 \\ Lxg_2 \end{Bmatrix}; \ \boldsymbol{T} = \{T_1, T_2, \ \ldots, T_l\}; \ l = n + m \tag{2}$$

where $\boldsymbol{C}_2$ represents the influence matrix corresponding to the change in length of the upper and lower units of the closure segment caused by a unit change in the initial tension of the stay cables in the maximum cantilever state of the unilateral cable-stayed system, $\boldsymbol{T}$ is a set of cable force values, T_l is the initial tension of the lth cable, Lxg_1 and Lxg_2 are the length changes of the upper and lower units of the closure segment under the dead load of the structure in the same state.

By substituting Eq. (2) into Eq. (1), the mechanical state connection equation between the pre-arching and post-arching stages is obtained, as expressed in Eq. (3):

$$\boldsymbol{C}_1\left\{\boldsymbol{C}_2\begin{Bmatrix} T_1 \\ T_2 \\ \vdots \\ T_l \end{Bmatrix} + \begin{Bmatrix} Lxg_1 \\ Lxg_2 \end{Bmatrix}\right\} = \begin{Bmatrix} hv_1 \\ hv_2 \\ \vdots \\ hv_n \end{Bmatrix} \tag{3}$$

3.1.2. Constraint equation

As shown in Fig. 2(b), the alignment constraint for the central arch rib is expressed in Eq. (4), derived in conjunction with Eq. (3) to satisfy the precision requirements of the arch alignment after formation. By rearranging Eq. (4), a simplified alignment constraint for the central arch rib is obtained, as shown in Eq. (5).

$$-\begin{Bmatrix} ta_1 \\ ta_2 \\ \vdots \\ ta_n \end{Bmatrix} \le \boldsymbol{C}_1\left\{\boldsymbol{C}_2\begin{Bmatrix} T_1 \\ T_2 \\ \vdots \\ T_l \end{Bmatrix} + \begin{Bmatrix} Lxg_1 \\ Lxg_2 \end{Bmatrix}\right\} \le \begin{Bmatrix} ta_1 \\ ta_2 \\ \vdots \\ ta_n \end{Bmatrix} \tag{4}$$

$$\boldsymbol{A}_1\boldsymbol{T} \le \boldsymbol{B}_1; \ \boldsymbol{A}_1 = \begin{bmatrix} \boldsymbol{C}_1\boldsymbol{C}_2 \\ -\boldsymbol{C}_1\boldsymbol{C}_2 \end{bmatrix}; \ \boldsymbol{B}_1 = \begin{Bmatrix} \boldsymbol{ta} - \boldsymbol{C}_1\begin{Bmatrix} Lxg_1 \\ Lxg_2 \end{Bmatrix} \\ \boldsymbol{ta} + \boldsymbol{C}_1\begin{Bmatrix} Lxg_1 \\ Lxg_2 \end{Bmatrix} \end{Bmatrix}; \ \boldsymbol{T} = \begin{bmatrix} T_1 \\ T_2 \\ \vdots \\ T_l \end{bmatrix}; \ \boldsymbol{ta} = \begin{bmatrix} ta_1 \\ ta_2 \\ \vdots \\ ta_n \end{bmatrix} \tag{5}$$

where $\boldsymbol{ta}$ is target vector, and ta_n represents the control limits for elevation errors at the measurement points of the central arch rib in the maximum cantilever state; $\boldsymbol{A}_1$ is generalized influence matrix, $\boldsymbol{B}_1$ is generalized objective vector.

Moreover, tower deviation is a critical parameter reflecting whether the cable-stayed towers remain in force equilibrium. Maintaining tower deviation within a prescribed range ensures the structural safety of the towers. Using the influence matrix method, a constraint equation is established to control tower deviation during cantilever construction of the cable-stayed system up to the ith construction stage. To account for the effect of initial cable tension on the actual cable forces under load at the ith stage, the influence matrix of the initial stay-cable tension on the true cable force is constructed, as shown in Eq. (6).

$$\begin{cases} -\boldsymbol{h}_{\mathrm{T}i} \le \boldsymbol{C}_{ki}\boldsymbol{T} - \boldsymbol{h}_{\mathrm{T}gi} \le \boldsymbol{h}_{\mathrm{T}i} \\ \boldsymbol{t}_{\min} \le \boldsymbol{C}_{xi}\boldsymbol{T} + \boldsymbol{t}_{gi} \le \boldsymbol{t}_{\max} \\ \boldsymbol{T} = \begin{bmatrix} T_1 \\ T_2 \\ \vdots \\ T_l \end{bmatrix}; \ \boldsymbol{h}_{\mathrm{T}i} = \begin{bmatrix} h_{\mathrm{T}i1} \\ h_{\mathrm{T}i2} \\ \vdots \\ h_{\mathrm{T}is} \end{bmatrix}; \ \boldsymbol{h}_{\mathrm{T}gi} = \begin{bmatrix} h_{\mathrm{T}gi1} \\ h_{\mathrm{T}gi2} \\ \vdots \\ h_{\mathrm{T}gis} \end{bmatrix}; \ \boldsymbol{t}_{gi} = \begin{bmatrix} t_{gi1} \\ t_{gi2} \\ \vdots \\ t_{gil} \end{bmatrix} \end{cases} \tag{6}$$

where $\boldsymbol{C}_{ki}$ represents the influence of changes in cable force on the tower deviation at the ith stage of cantilever construction in the cable-stayed system, $\boldsymbol{C}_{xi}$ is the influence matrix of the initial cable tension on the true cable forces during cantilever construction up to the ith stage, $\boldsymbol{t}_{\min}$ is the minimum allowable true cable force, and $\boldsymbol{t}_{\max}$ is the maximum allowable true cable force. For closure backstay cables that have not yet been constructed in subsequent stages, the corresponding terms are taken as zero when the cantilever construction reaches the ith stage, $\boldsymbol{h}_{\mathrm{T}i}$ is the tower deviation control vector during cantilever construction up to the ith stage, $h_{\mathrm{T}is}$ is the deviation of the sth control point of the tower during cantilever construction up to the ith stage, $\boldsymbol{h}_{\mathrm{T}gi}$ is the influence vector of the tower's self-weight deviation during cantilever construction up to the ith stage, $h_{\mathrm{T}gis}$ is the tower deviation at the sth control point of the tower during cantilever construction up to the ith stage, $\boldsymbol{t}_{gi}$ is The influence vector of the self-weight of the tower on the cable force during cantilever construction up to the ith stage, t_{gil} is the change in the true cable force of the lth stay cable due to self-weight during cantilever construction up to the ith stage.

A simplified constraint for tower deviation, given in Eq. (7), can be derived from Eq. (6) to ensure optimal tower deviation control during the cantilever construction stage of the cable-stayed system.

$$\boldsymbol{A}_i'\boldsymbol{T} \le \boldsymbol{B}_i'; \ \boldsymbol{A}_i' = \begin{bmatrix} \boldsymbol{C}_{ki} \\ -\boldsymbol{C}_{ki} \\ \boldsymbol{C}_{xi} \\ -\boldsymbol{C}_{xi} \end{bmatrix}; \ \boldsymbol{B}_i' = \begin{bmatrix} \boldsymbol{h}_{\mathrm{T}i} + \boldsymbol{h}_{\mathrm{T}gi} \\ \boldsymbol{h}_{\mathrm{T}i} - \boldsymbol{h}_{\mathrm{T}gi} \\ \boldsymbol{t}_{\max} - \boldsymbol{t}_{gi} \\ -\boldsymbol{t}_{\min} + \boldsymbol{t}_{gi} \end{bmatrix} \tag{7}$$

where $\boldsymbol{A}_i'$ is generalized tower deviation influence matrix during cantilever construction up to the ith stage, $\boldsymbol{B}_i'$ is the generalized tower deviation target vector for cantilever construction up to the ith stage.

Finally, the constraints on the alignment deviation after arch formation, tower deviation, and allowable cable force range are integrated, as expressed in Eq. (8).

$$\boldsymbol{A}\boldsymbol{T} \le \boldsymbol{B}; \ \boldsymbol{A} = \left[\boldsymbol{A}_1, \boldsymbol{A}_1', \boldsymbol{A}_2', \ \ldots, \boldsymbol{A}_i'\right]^{\mathrm{T}}; \ \boldsymbol{B} = \left[\boldsymbol{B}_1, \boldsymbol{B}_1', \boldsymbol{B}_2', \ \ldots, \boldsymbol{B}_i'\right]^{\mathrm{T}} \tag{8}$$

where $\boldsymbol{A}$ is generalized tower deviation influence matrix, $\boldsymbol{B}$ is generalized tower deviation control matrix.

Additional constraints, such as stress-free length and curvature requirements during the closure stage, can also be incorporated into Eq. (8).

3.1.3. Objective function

An objective function is formulated to minimize the variation of cable forces, as shown in Eq. (9), in order to control fluctuations in local stress and maintain the structural alignment of the cable-stayed towers and main arch throughout the construction process, as illustrated in Fig. 2(c).

$$\min\left\{\mathrm{CV}=\frac{\sigma}{\mu}\times 100\%\right\} \tag{9}$$

where CV is the cable force variation coefficient, μ represents the average cable force, which is $\mu=\frac{1}{l}\sum_{i=1}^{l}T_i$; σ represents the variance of the cable force, which is $\sigma=\sqrt{\frac{1}{l}\sum_{i=1}^{l}(T_i-\mu)^2}$.

3.1.4. Optimization model solving

Using the constraints in Eq. (8) and the objective in Eq. (9), the problem of controlling alignment throughout the construction of the central arch rib of a large-span arch bridge is formulated as a multi-constraint optimization problem. A nondominated genetic algorithm [39] is employed to determine a set of cable forces that minimize the main arch rib alignment error, maintain tower deviation within allowable limits, and ensure reasonable cable force distribution.

3.2. Precise manufacturing for rib segments

Prefabricated arch rib segments inevitably contain manufacturing errors, including material dimensional deviations, cutting and blanking inaccuracies, welding imperfections, and fabrication-induced deformations. Traditionally, multiple rounds of physical preassembly have been employed to compensate for these geometric errors and ensure proper alignment when assembling multiple segments into the full arch. However, this approach demands substantial labor, large staging areas, and heavy equipment. To address these limitations, a manufacturing control method based on digital preassembly is proposed. This method allows independently fabricated segments, despite inherent errors, to be virtually joined in a digital environment, ensuring that the full arch achieves the designed alignment with high precision. The detailed stepwise framework of this approach is illustrated in Fig. 3.

3.2.1. Acquisition of a high-fidelity model of a precast segment

The alignment point clouds of precast arch rib segments without installed flanges are captured at multiple locations using a 3D laser scanner, as shown in Fig. 3(a). A fine registration process is then performed on the multistation point cloud scans, which consists of two steps: coarse and fine registrations. Mature algorithms [40–42] can be applied for coarse registration. After this step, slight misalignments between point clouds often remain. To resolve these, the iterative closest point (ICP) algorithm [43] is used for local registration, producing a high-fidelity scanned point cloud model of the arch rib segments, as shown in Fig. 3(b).

3.2.2. Digital assembly of the segment model

A methodology for digitally assembling arch rib point clouds with the as-designed BIM is proposed, incorporating a double-weighted alignment approach, as illustrated in Fig. 3(c). First, the semantic and distribution weights of the arch rib point cloud are determined. The semantic weight of each component w_{1i}, $w_{1i}\in(0,1)$, is assigned based on its importance within the segment, with the main chord typically weighted at 0.7 and other components weighted between 0.3 and 0.5. Second, the longitudinal direction of each bar's point cloud is calculated using principal component analysis (PCA), and the chord point cloud is divided into five regions along this axis. The outer and inner regions are assigned smaller distribution weights to account for their reduced structural significance. The point cloud distribution weights for each region, w_{2i} and $w_{2i}\in(0,1)$, are set as 0.5 for the outermost region, 0.2 for the middle region, and 0.3 for the remaining regions. A schematic of the point cloud semantics and distribution weights is shown in Fig. 4(a).

Following weight assignment, the arch rib point cloud is aligned with the as-designed BIM. Components of the BIM, excluding the flange, are densely sampled to form a corresponding point cloud. A double-weighted least-squares objective function is then established to minimize alignment errors between the scanned point cloud and the BIM, as defined in Eq. (10):

$$E(\boldsymbol{R},\boldsymbol{Tr})=\sum\nolimits_i w_{1i}w_{2i}\|\boldsymbol{R}\cdot\boldsymbol{p}_i+\boldsymbol{Tr}-\boldsymbol{q}_i\| \tag{10}$$

where $\boldsymbol{R}$ is the rotation matrix, and $\boldsymbol{Tr}$ is the translation matrix. $\boldsymbol{p}_i$ represents the scanned point cloud vector of the arch rib segment, and $\boldsymbol{q}_i$ denotes the sampled point cloud vector from the design BIM model. The K-dimensional tree algorithm is employed to find the corresponding points in $\{\boldsymbol{p}_i\}$ and $\{\boldsymbol{q}_i\}$ to speed up the nearest corresponding point search. After constructing the weighted centroids of the point clouds, the data are centralized as shown in Eqs. (11)–(14).

$$\bar{\boldsymbol{p}}_{\mathrm{w}}=\frac{\sum_i w_{1i}w_{2i}\boldsymbol{p}_i}{\sum_i w_{1i}w_{2i}} \tag{11}$$

$$\bar{\boldsymbol{q}}_{\mathrm{w}}=\frac{\sum_i w_{1i}w_{2i}\boldsymbol{q}_i}{\sum_i w_{1i}w_{2i}} \tag{12}$$

$$\boldsymbol{p}_{\mathrm{w}i}=\boldsymbol{p}_i-\bar{\boldsymbol{p}}_{\mathrm{w}} \tag{13}$$

$$\boldsymbol{q}_{\mathrm{w}i}=\boldsymbol{q}_i-\bar{\boldsymbol{q}}_{\mathrm{w}} \tag{14}$$

where $\bar{\boldsymbol{p}}_{\mathrm{w}}$ and $\bar{\boldsymbol{q}}_{\mathrm{w}}$ denote the double-weighted centroids of the arch rib scanned point cloud $\{\boldsymbol{p}_i\}$ and the design BIM sampled point cloud $\{\boldsymbol{q}_i\}$, respectively. $\boldsymbol{p}_{\mathrm{w}i}$ and $\boldsymbol{q}_{\mathrm{w}i}$ are the decentered scanned and BIM point clouds after accounting for double weights. A double-weighted covariance matrix $\boldsymbol{S}$ is constructed from the decentered point clouds, as shown in Eq. (15). Singular value decomposition (SVD) of $\boldsymbol{S}$ is then performed to obtain the rotation matrix $\boldsymbol{R}_j$ and translation matrix $\boldsymbol{Tr}_j$, as indicated in Eq. (16):

$$\boldsymbol{S}=\sum\nolimits_i w_{1i}w_{2i}\boldsymbol{p}_{\mathrm{w}i}\boldsymbol{q}_{\mathrm{w}i}{}^{\mathrm{T}} \tag{15}$$

$$\boldsymbol{S}=\boldsymbol{U}\sum\boldsymbol{V}^{\mathrm{T}};\ \boldsymbol{R}_j=\boldsymbol{U}\boldsymbol{V}^{\mathrm{T}};\ \boldsymbol{Tr}_j=\bar{\boldsymbol{q}}_{\mathrm{w}}-\boldsymbol{R}_j\bar{\boldsymbol{p}}_{\mathrm{w}} \tag{16}$$

where $\boldsymbol{U}$ and $\boldsymbol{V}$ are the orthogonal matrices from the SVD, and $\sum$ is the diagonal matrix of singular values. The rotation matrix $\boldsymbol{R}_j$ and translation matrix $\boldsymbol{Tr}_j$ are iteratively updated until the double-weighted objective error function reaches a preset threshold or the maximum number of iterations is achieved. The final rotation matrix $\boldsymbol{R}$ and translation matrix $\boldsymbol{Tr}$ provide the accurate alignment of the scanned arch rib point cloud with the as-designed BIM, as illustrated in Fig. 4(b).

3.2.3. Manufacturing alignment control

The alignment of all arch ribs after digital assembly is obtained by aligning the scanned point clouds of all segments with the as-designed BIM. The relative attitude of adjacent arch rib segments defines the splicing relationship used during subsequent manufacturing. This splicing relationship serves as the control target for positioning the arch rib segments and flange during actual fabrication, as shown in Fig. 3(d).

3.3. Automatic adjustment for the installation of arch rib segments

An automatic installation attitude adjustment strategy based on original-shape restoration is proposed to improve the precision

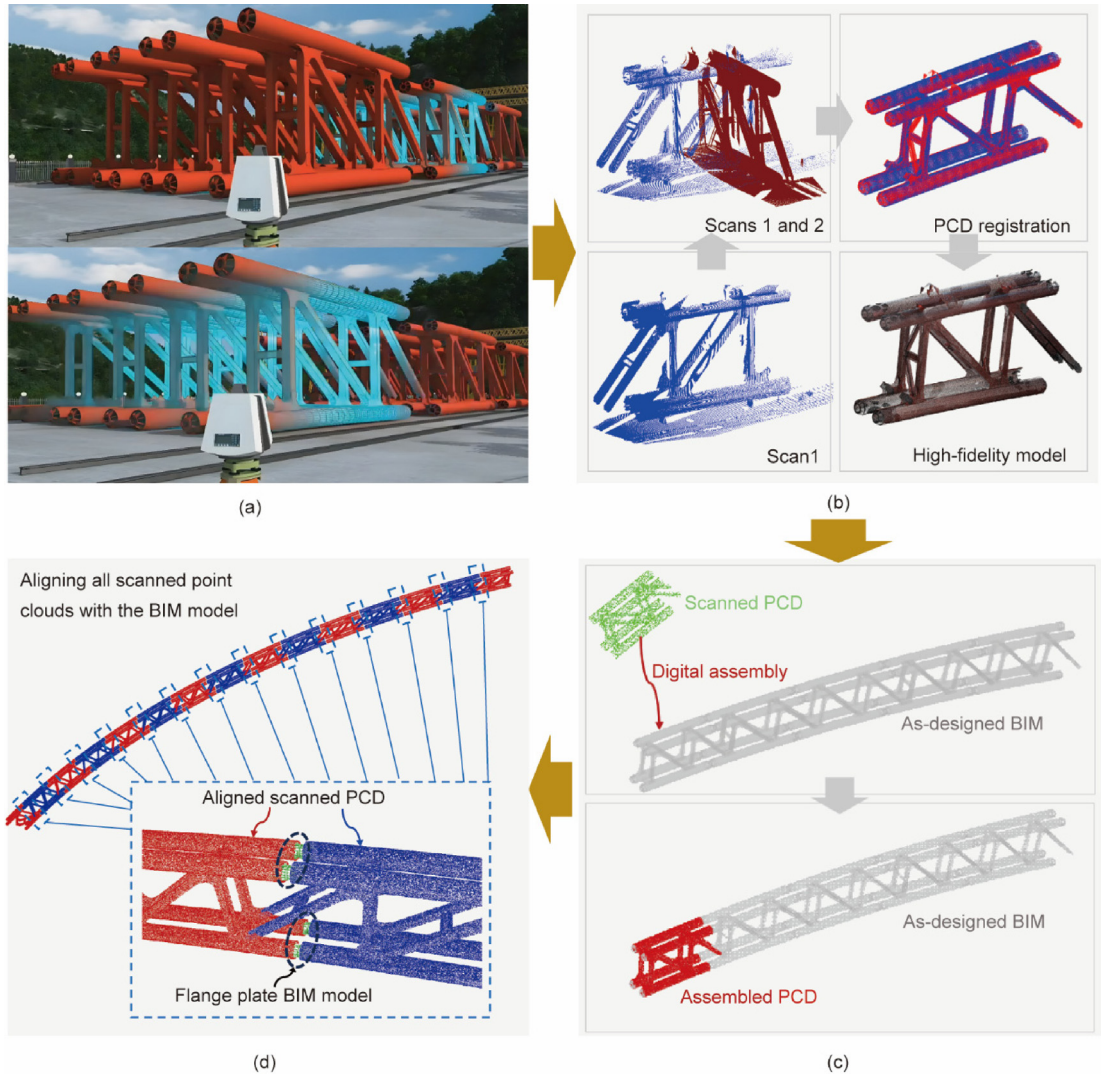

Fig. 3. Implementation steps of the digital preassembly control method for arch rib segments. (a) Scanning arch rib segments; (b) acquiring high-fidelity point cloud data (PCD) models; (c) digitally assembling the PCD with BIM; (d) determining the splicing relationship of adjacent segments to guide the manufacturing process.

and efficiency of arch rib segment installation. Original-shape restoration maintains the relative spatial relationships among segments established during the manufacturing stage. The key steps are illustrated in Fig. 5 and are as follows: ① During manufacturing, a high-fidelity 3D point cloud of the completed arch rib is captured using 3D laser scanning; ② this point cloud is treated as the baseline original shape, and the no-load installation attitude of each arch rib segment is determined by transforming from the manufacturing coordinate system to the installation coordinate system; ③ deformations caused by self-weight and temperature loads are superimposed on the no-load attitude to compute the target installation attitude; ④ the point cloud of the initial installation attitude is acquired; and ⑤ a 3D deviation analysis between the initial and target installation attitudes is performed to generate the attitude adjustment strategy, enabling precise one-time adjustment and positioning of each arch rib segment.

3.3.1. Acquisition of the target attitude for arch rib installation

The point cloud of the arch rib in its manufacturing attitude, $\boldsymbol{P}_{\mathrm{A}}$, including manufacturing errors, is captured using 3D laser scanning within the manufacturing coordinate system and is used as the baseline original shape. Transforming $\boldsymbol{P}_{\mathrm{B}}$ from the manufacturing coordinate system to the installation coordinate system yields the no-load target installation attitude, $\boldsymbol{P}_{\mathrm{B}}$, as shown in Fig. 5(a):

$$\boldsymbol{P}_{\mathrm{B}} = \boldsymbol{T}\boldsymbol{p}_1 \boldsymbol{P}_{\mathrm{A}} \tag{17}$$

$$\boldsymbol{T}\boldsymbol{p}_1 = \begin{bmatrix} \boldsymbol{R}_1 & \boldsymbol{t}\boldsymbol{p}_1 \\ 0 & 1 \end{bmatrix} \tag{18}$$

where $\boldsymbol{T}\boldsymbol{p}_1$ is a 4 × 4 transformation matrix composed of a 3 × 3 rotation matrix $\boldsymbol{R}_1$ and a 3 × 1 translation vector $\boldsymbol{t}\boldsymbol{p}_1$, obtained through coordinate transformation.

To account for deformations caused by self-weight and temperature loads during installation, the attitude transformation matrix $\boldsymbol{T}\boldsymbol{p}_2$ before and after loading is computed, as expressed in Eq. (19):

$$\boldsymbol{T}\boldsymbol{p}_2 = \begin{bmatrix} \boldsymbol{R}_2 & \boldsymbol{t}\boldsymbol{p}_2 \\ 0 & 1 \end{bmatrix} \tag{19}$$

First, using a finite element model, the original coordinates $\boldsymbol{P}_{\mathrm{C}}$ and deformed coordinates $\boldsymbol{P}_{\mathrm{D}}$ of all nodes of the arch rib segment after loading are obtained. Next, let $\boldsymbol{t}\boldsymbol{p}_2$ denote the translation vector, $\boldsymbol{R}_2$ the rotation matrix, c the scale factor, and $\boldsymbol{j}$ an auxiliary unit vector. A diagonal weight matrix $\boldsymbol{W}$ is introduced to assign different weights based on point precision. The minimum-value function is then constructed using the EOPA method [20], as detailed in the following formula:

$$\mathrm{tr}\left[\boldsymbol{H}^{\mathrm{T}}\boldsymbol{W}^2\boldsymbol{H}\right] = \min;\ \boldsymbol{H} = \boldsymbol{P}_{\mathrm{D}} - c\boldsymbol{P}_{\mathrm{C}}\boldsymbol{R}_2 - \boldsymbol{j}\boldsymbol{t}\boldsymbol{p}_2{}^{\mathrm{T}} \tag{20}$$

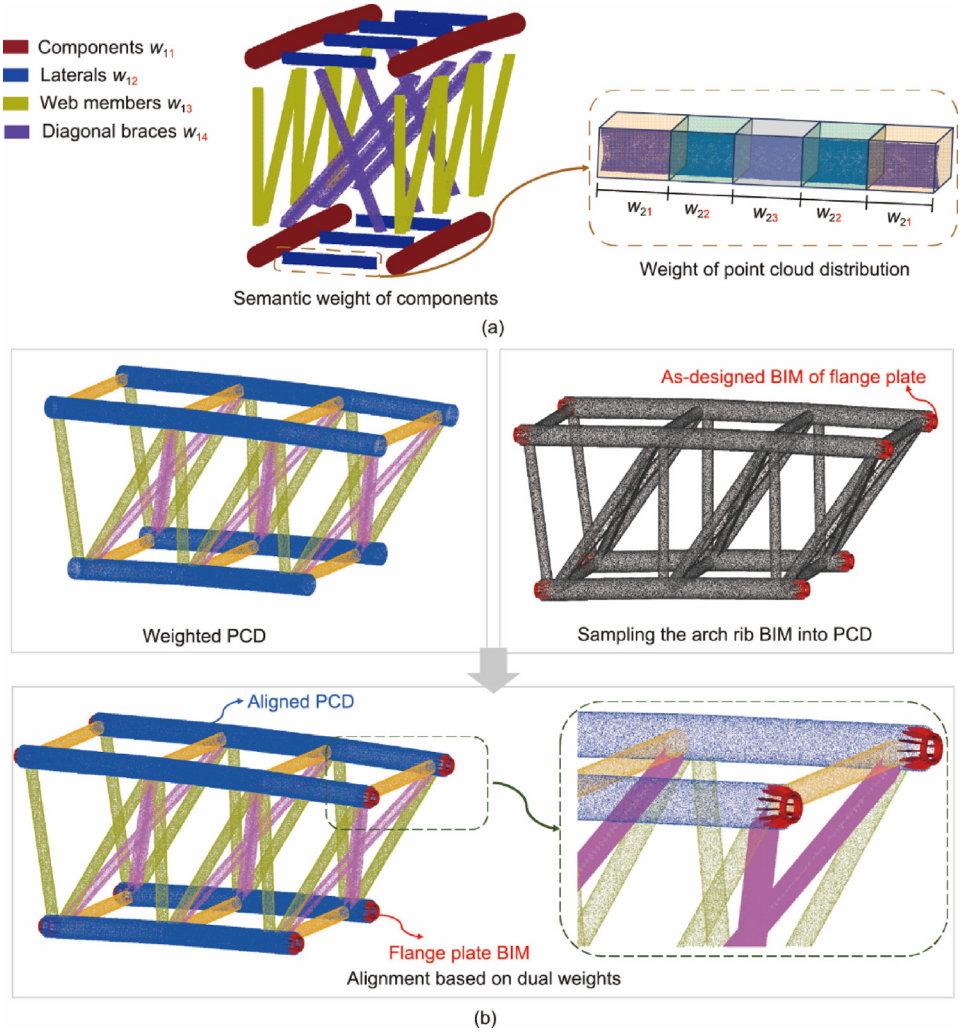

Fig. 4. Digital assembly of the arch rib PCD with the as-designed BIM: (a) illustration of PCD semantic and distribution weights; (b) detailed process of precise alignment.

where $\boldsymbol{H}$ is the optimized orthogonal projection matrix. The matrix can be decomposed using Cholesky factorization, as shown in Eq. (21):

$$\boldsymbol{W}=\boldsymbol{Q}^{\mathrm{T}}\boldsymbol{Q};\ \boldsymbol{I}_{\mathrm{W}}=\left(\boldsymbol{I}-\frac{\boldsymbol{j}_{\mathrm{W}}\boldsymbol{j}_{\mathrm{W}}^{\mathrm{T}}}{\boldsymbol{j}_{\mathrm{W}}^{\mathrm{T}}\boldsymbol{j}_{\mathrm{W}}}\right);\ \boldsymbol{P}_{\mathrm{CW}}=\boldsymbol{Q}\boldsymbol{P}_{\mathrm{C}},\ \boldsymbol{P}_{\mathrm{DW}}=\boldsymbol{Q}\boldsymbol{P}_{\mathrm{D}},\ \boldsymbol{j}_{\mathrm{W}}=\boldsymbol{Q}\boldsymbol{j} \tag{21}$$

where $\boldsymbol{Q}$ is the Cholesky decomposition matrix, $\boldsymbol{I}$ is the identity matrix; $\boldsymbol{I}_{\mathrm{W}}$ is the orthogonal projection onto the orthogonal complement of the vector $\boldsymbol{j}_{\mathrm{W}}$. $\boldsymbol{P}_{\mathrm{CW}}$ and $\boldsymbol{P}_{\mathrm{DW}}$ are the weighted-transformed matrices of $\boldsymbol{P}_{\mathrm{C}}$ and $\boldsymbol{P}_{\mathrm{D}}$, and $\boldsymbol{j}_{\mathrm{W}}$ is the weighted imaginary correction vector. In the final step, the translation vector $\boldsymbol{tp}_2$ and rotation matrix $\boldsymbol{R}_2$ can be obtained by conducting the spectral decomposition of the matrix product, as shown in Eqs. (22) and (23):

$$\boldsymbol{P}_{\mathrm{CW}}{}^{\mathrm{T}}\boldsymbol{I}_{\mathrm{W}}\boldsymbol{P}_{\mathrm{DW}}=\boldsymbol{V}_1\boldsymbol{D}_{\mathrm{S}}\boldsymbol{W}_1{}^{\mathrm{T}} \tag{22}$$

$$c=\frac{\mathrm{tr}\left[\boldsymbol{T}\boldsymbol{p}_2{}^{\mathrm{T}}\boldsymbol{P}_{\mathrm{CW}}{}^{\mathrm{T}}\boldsymbol{I}_{\mathrm{W}}\boldsymbol{P}_{\mathrm{DW}}\right]}{\mathrm{tr}\left[\boldsymbol{P}_{\mathrm{CW}}{}^{\mathrm{T}}\boldsymbol{I}_{\mathrm{W}}\boldsymbol{P}_{\mathrm{DW}}\right]};\ \boldsymbol{R}_2=\boldsymbol{V}_1\boldsymbol{W}_1{}^{\mathrm{T}};\ \boldsymbol{tp}_2=(\boldsymbol{P}_{\mathrm{DW}}-c\boldsymbol{P}_{\mathrm{CW}}\boldsymbol{R}_2)^{\mathrm{T}}\frac{\boldsymbol{j}_{\mathrm{W}}}{\boldsymbol{j}_{\mathrm{W}}{}^{\mathrm{T}}\boldsymbol{j}_{\mathrm{W}}} \tag{23}$$

where $\boldsymbol{V}_1$ and $\boldsymbol{W}_1$ are the decomposed orthogonal matrices, and $\boldsymbol{D}_{\mathrm{S}}$ is the decomposed diagonal matrix. Finally, the target attitude for installing the arch ribs $\boldsymbol{P}_{\mathrm{E}}$ can be obtained using Eq. (24), as follows:

$$\boldsymbol{P}_{\mathrm{E}}=\boldsymbol{T}\boldsymbol{p}_2\boldsymbol{P}_{\mathrm{B}}=\begin{bmatrix}\boldsymbol{R}_2 & \boldsymbol{tp}_2\\ 0 & 1\end{bmatrix}\boldsymbol{P}_{\mathrm{B}} \tag{24}$$

3.3.2. Acquisition of the attitude adjustment transformation matrix

After the arch rib segment is transported to the bridge site and preliminarily installed, its initial installation attitude point cloud, $\boldsymbol{P}_{\mathrm{F}}$, is captured using 3D laser scanning. Based on PCA, $\boldsymbol{P}_{\mathrm{F}}$ is registered with the target attitude for installing the arch ribs $\boldsymbol{P}_{\mathrm{E}}$ to determine the attitude adjustment transformation matrix, as illustrated in Fig. 5(b). The procedure is as follows:

First, the centroids of the point clouds $\boldsymbol{P}_{\mathrm{F}}$ and $\boldsymbol{P}_{\mathrm{E}}$ are calculated as follows:

$$\mathrm{centroid}_1=\frac{1}{n_1}\sum_{i=1}^{n_1}\boldsymbol{P}_{\mathrm{F}i};\ \mathrm{centroid}_2=\frac{1}{n_2}\sum_{i=1}^{n_2}\boldsymbol{P}_{\mathrm{E}i} \tag{25}$$

where n_1 is the number of point clouds in the initial installation posture, n_2 is the number of point clouds in the target installation posture; $\boldsymbol{P}_{\mathrm{E}i}$ and $\boldsymbol{P}_{\mathrm{F}i}$ are the coordinates of the ith point cloud in the initial and target installation postures, respectively. Subsequently, the transformation matrix is calculated, as shown in Eqs. (26) and (27):

$$\boldsymbol{P}'_{\mathrm{F}i}=\boldsymbol{P}_{\mathrm{F}i}-\mathrm{centroid}_1;$$
$$\boldsymbol{P}'_{\mathrm{E}i}=\boldsymbol{P}_{\mathrm{E}i}-\mathrm{centroid}_2;\ \frac{1}{n_3}\sum_{i=1}^{n_3}\boldsymbol{P}'_{\mathrm{F}i}\left(\boldsymbol{P}'_{\mathrm{E}i}\right)^{\mathrm{T}}=\boldsymbol{V}_2\sum\boldsymbol{W}_2{}^{\mathrm{T}} \tag{26}$$

$$\boldsymbol{Tp}_3 = \begin{bmatrix} \boldsymbol{R}_3 & \boldsymbol{tp}_3 \\ 0 & 1 \end{bmatrix};\ \boldsymbol{R}_3 = \boldsymbol{W}_2\boldsymbol{V}_2{}^{\mathrm{T}},\ \boldsymbol{tp}_3 = \mathrm{centroid}_2 - \boldsymbol{R}_3 \cdot \mathrm{centroid}_1 \tag{27}$$

where n_3 is the number of matched point clouds between the initial posture and target installation posture.$\boldsymbol{P}'_{Fi}$ and $\boldsymbol{P}'_{Ei}$ are the decentralized point cloud coordinates of $\boldsymbol{P}_{Ei}$ and $\boldsymbol{P}_{Fi}$. $\boldsymbol{V}_2$ and $\boldsymbol{W}_2$ are the decomposed orthogonal matrices, and $\boldsymbol{tp}_3$ is the translation vector in the transformation process. To facilitate the subsequent attitude adjustment model construction, the transformation matrix $\boldsymbol{Tp}_3$ is generally represented as follows:

$$\boldsymbol{Tp}_3 = \begin{bmatrix} R_{31} & R_{32} & R_{33} & tp_{31} \\ R_{34} & R_{35} & R_{36} & tp_{32} \\ R_{37} & R_{38} & R_{39} & tp_{33} \\ 0 & 0 & 0 & 1 \end{bmatrix} \tag{28}$$

where $R_{31}, \ldots, R_{39}$ are the rotation transformation parameters; tp_{p31}, $\ldots$, tp_{33} are the translation transformation parameters.

3.3.3. Fine adjustment of segment attitude

The installation of arch rib segments is divided into two construction stages based on the methods employed in the small cantilever and large cantilever phases. In the small cantilever stage, the self-weight of the arch rib segments is supported by ground supports (Fig. 5(c)), whereas in the large cantilever stage, cable-stayed fastening–hanging construction is used (Fig. 5(d)). For the small cantilever stage, four jacks with three-direction adjustment capability are installed at the contact points between the arch rib segment and the support to apply the required corrections.

In the initial installation attitude point cloud $\boldsymbol{P}_F$, one point is selected at the contact surface corresponding to each of the four jacks to form the contact-point coordinate matrix $\boldsymbol{D}_1 = [x_i, y_i, z_i, 1]^{\mathrm{T}}\ (i = 1, 2, 3, 4)$. After transformation using the attitude adjustment matrix $\boldsymbol{Tp}_3$, the adjusted contact-point coordinate matrix $\boldsymbol{D}'_1 = [x'_i, y'_i, z'_i, 1]^{\mathrm{T}} (i = 1, 2, 3, 4)$ is obtained. The adjustment quantities for each 3D jack are then computed as:

$$\Delta\boldsymbol{D}_1 = \boldsymbol{D}'_1 - \boldsymbol{D}_1 \tag{29}$$

This establishes a mathematical solution model relating the manufacturing attitude of the arch rib segment, the initial installation attitude, and the 3D jack adjustment quantities, enabling precise and rapid posture correction under the floor-support construction condition.

For the large cantilever stage with cable-stayed construction, the backstay, wind-resistant, and other cable members serve as the adjustment mechanisms. In the initial installation attitude point cloud $\boldsymbol{P}_F$, a coordinate matrix $\boldsymbol{D}_2 = [x_j, y_j, z_j, 1]^{\mathrm{T}} (j = 1, 2, 3, 4)$ is formed using two points at the front and back of each installed arch rib segment. Similarly, the adjusted coordinate matrix $\boldsymbol{D}'_2$ and the adjustment quantity matrix $\Delta\boldsymbol{D}_2$ are obtained. The solution is obtained by reassembling $\Delta\boldsymbol{D}_2$, thereby obtaining the final adjustment quantity matrix $\Delta\boldsymbol{D}'_2 = [\Delta x_j, \Delta y_j, \Delta z_j]^{\mathrm{T}} (j = 1, 2, 3, 4)$. Let the cable force adjustment matrix be $\boldsymbol{L} = [L_1 \quad L_2 \quad \cdots \quad L_m]^{\mathrm{T}}$. The influence relationship $\Delta\boldsymbol{D}'_2$ between the unit change of each tension member and the coordinates of points in $\boldsymbol{K}_2$ is established, as expressed in Eqs. (30) and (31).

$$\boldsymbol{K}_2 \cdot \boldsymbol{L} = \Delta\boldsymbol{D}'_2 \tag{30}$$

$$\boldsymbol{K}_2 = \begin{bmatrix} L_{1\Delta x_1} & L_{2\Delta x_1} & \cdots & L_{m\Delta x_1} \\ L_{1\Delta y_1} & L_{2\Delta y_1} & \cdots & L_{m\Delta y_1} \\ \cdots & \cdots & \cdots & \cdots \\ L_{1\Delta z_4} & L_{2\Delta z_4} & \cdots & L_{m\Delta z_4} \end{bmatrix} \tag{31}$$

where L_m denotes the adjustment quantity of the force in the mth cable; $\boldsymbol{K}_2$ is the matrix of the influence relationship between cable variation and final adjustment variation. $L_{m\Delta x_i}$, $L_{m\Delta y_i}$, and $L_{m\Delta z_i}$

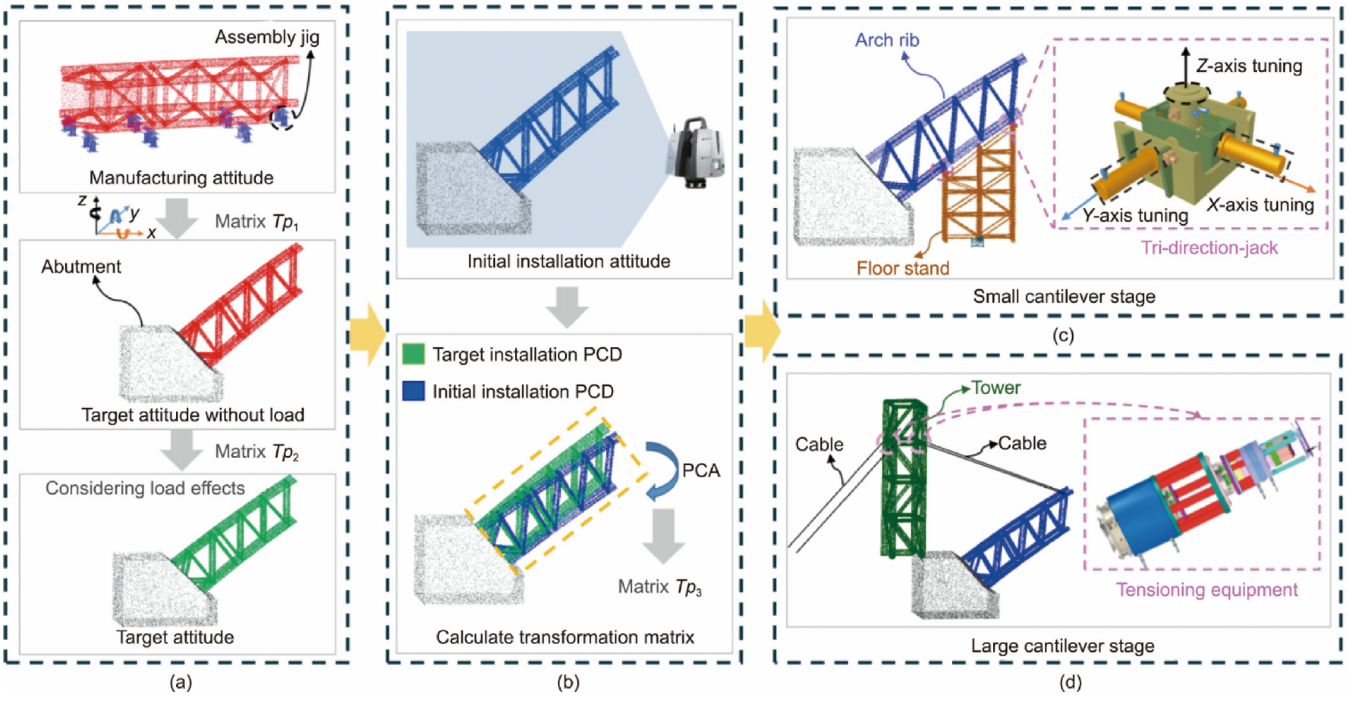

Fig. 5. Automatic adjustment process for arch rib installation attitude: (a) acquisition of installation attitude; (b) attitude adjustment transformation matrix; (c) schematic of small-cantilever stage construction; and (d) schematic of large-cantilever stage construction.

denote the change quantities Δx_j, Δy_j, and Δz_j, respectively, caused by a unit change in the force of the mth cable.

At this point, the cable force adjustment quantity matrix $\boldsymbol{L}$ may not have an exact solution. The singular value is used to obtain the minimum solution of the least squares.

$$\boldsymbol{K}_2 = \boldsymbol{V}_4 \sum \boldsymbol{W}_4^{\mathrm{T}};\ \boldsymbol{L} = \boldsymbol{W}_4 \sum\nolimits^{+} \boldsymbol{V}_4^{\mathrm{T}} \boldsymbol{T}_4 \tag{32}$$

where $\boldsymbol{V}_4$ is the left singular matrix of $\boldsymbol{K}_2$, $\boldsymbol{W}_4$ is the correct singular matrix of $\boldsymbol{K}_2$, and $\sum^{+}$ is the pseudoinverse matrix of $\sum$.

In summary, the mathematical model for adjusting the installation attitude of the arch rib segments under two operating modes has been completed, enabling precise adjustment in a one-time operation of all arch rib segments.

4. Engineering applications

4.1. Engineering overview

To validate the accuracy and applicability of the proposed method, tests were conducted on a super-long-span concrete-filled steel tube (CFST) arch bridge, the Deyu Expressway Wujiang Bridge, located in Guizhou Province, China. The main arch rib spans 504 m, with a rise of 90 m and an arch-axis coefficient of 2.2, as shown in Fig. 6. Bolted connections are used for the main arch, columns, and deck girders to enhance construction speed and quality under the challenging mountainous conditions. Flange connections are employed between arch ribs, and the full arch consists of 32 segments, including the closure segment. All segments were fabricated at a steel fabrication base in Chongqing and transported by waterway to the bridge site. At the site, the wharf served as the assembly yard, and four rounds of physical preassembly were conducted for the arch rib segments on each bank.

The cable-stayed fastening–hanging system of the Deyu Expressway Wujiang Bridge includes 30 sets of anchor cables on both banks, anchor towers on each bank, and six anchor blocks, as illustrated in Fig. 7. The bridge is located on the northern edge of the Guizhou Plateau within a typical U-shaped valley. Construction involved prolonged work at height in a complex mountainous environment, resulting in high risk. Furthermore, to ensure reliable bolting of all components, stringent requirements were imposed on the manufacturing alignment of the arch rib segments and on their installation accuracy.

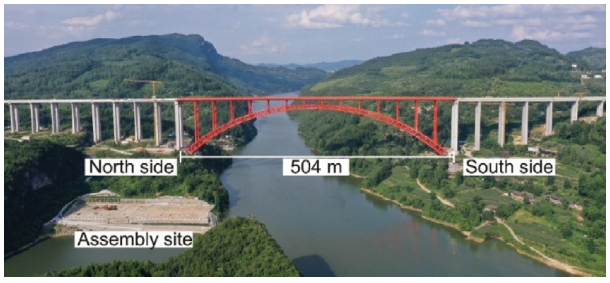

Fig. 6. Photograph of the Deyu Expressway Wujiang Bridge.

4.2. Implementation steps

4.2.1. Arch-forming model establishment and cable force calculation

Using the OpenSeesPy finite element analysis platform (Oregon State University, USA), both the maximum cantilever model and the bare arch model of the Deyu Expressway Wujiang Bridge were developed to determine the optimal cable force scheme across all construction stages, as shown in Fig. 8. In the bare arch model, the influence matrix $\boldsymbol{C}_1$ representing the effect of closure segment deformation on the elevation of various control points is obtained by applying forced strain to the closure segment, as described in Eq. (1). For the maximum cantilever model, the influence matrix $\boldsymbol{C}_2$ capturing the effect of individual cable forces on the elevation of control points is obtained by varying the force of a single cable, as shown in Eq. (3). The deformation dxg of the closure segment under self-weight alone is also determined. For the maximum cantilever model, models for each cantilever construction stage are generated sequentially. From these models, the influence matrix $[\boldsymbol{C}_{k1}, \boldsymbol{C}_{k2}, \ldots, \boldsymbol{C}_{kw}]$ of cable force on the tower deviation and the influence matrix $[\boldsymbol{C}_{x1}, \boldsymbol{C}_{x2}, \ldots, \boldsymbol{C}_{xw}]$ of initial cable tension on cable forces are extracted, as presented in Eq. (6).

Using the whole-process arch optimization control method developed in this study, the constraint Eq. (8) for alignment deviation after arching, tower deviation control, and cable force limits, along with the objective Eq. (9) minimizing the variation coefficient of cable forces, are established. Solving this multiconstraint optimization problem yields a set of cable forces that ensure minimal main arch rib alignment deviation, compliance with tower deviation standards, and reasonable cable force distribution for the large-span arch bridge.

4.2.2. Manufacturing alignment control of the arch rib manufacturing

The methodology described in this section is demonstrated using segments 11–15 on the south bank of the Wujiang Bridge. The actual point cloud of the arch ribs was captured using a TLS at the arch rib storage site, with a total of 33 scanning stations. The arrangement of the scanning stations is schematically shown in Fig. 9(a). The scanned point cloud was then aligned in two stages: First, a coarse registration was performed, followed by a fine registration using the ICP algorithm. The high-fidelity point cloud of the arch rib segments was distinguished and numbered, as shown in Fig. 9(b).

Subsequently, the semantic weights of the scanned arch rib segments and the point cloud distribution weights were defined. In this example, the main chord was assigned a semantic weight of 0.7, while the remaining chords were assigned a weight of 0.3, as illustrated in Fig. 9(c). The point cloud of each chord was divided into five regions along its length, with weights assigned as 0.5 for the outermost region, 0.2 for the middle region, and 0.3 for

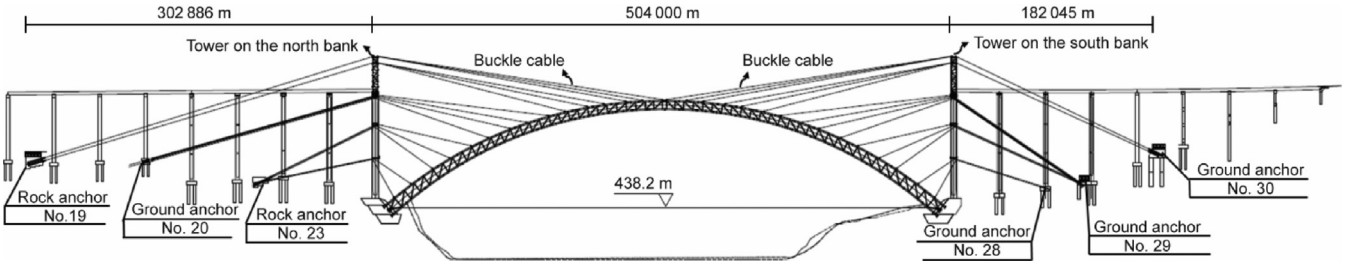

Fig. 7. General layout of the cable-stayed system of the Deyu Expressway Wujiang Bridge.

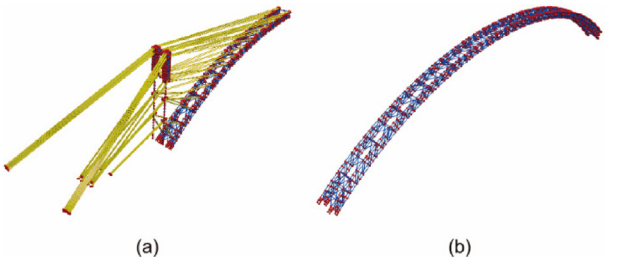

Fig. 8. Finite element model based on OpenSeesPy. (a) Maximum cantilever model; (b) naked arch model.

the remaining regions, as shown in Fig. 9(d). The components of arch ribs 11–15 in the as-designed BIM, excluding the flange, were initially sampled at high density using the proposed double-weighted point cloud–BIM alignment method. The scanned point cloud and the BIM-sampled point cloud were digitally assembled to determine the splicing relationships of segments 11–15, as illustrated in Fig. 9(e). The actual arch rib segments were then connected to the flange according to this splicing relationship.

4.2.3. Attitude adjustment of the arch ribs

This section illustrates the method using the installation of the first segments of the Wujiang Bridge as an example. After completing the attitude adjustment of the first segment's physical assembly, a scanning station is established to capture the point cloud of the manufacturing attitude of the arch rib $\boldsymbol{P}_A$, as shown in Figs. 10(a) and (b). The transformation matrix $\boldsymbol{T}_1$ is obtained by relating the coordinate system of the preassembly site to the on-site installation. After the point cloud $\boldsymbol{P}_A$ is transformed, the installation target attitude under no-load conditions, $\boldsymbol{P}_B$, is obtained.

Once the arch rib segments are transported to the bridge site, the initial installation attitude point cloud, $\boldsymbol{P}_F$, is obtained, as shown in Figs. 10(c) and (d). The measured temperature of the arch rib segments is recorded, and the point cloud $\boldsymbol{P}_B$ is adjusted to account for self-weight and temperature loads to obtain the target installation attitude for the first segment, $\boldsymbol{P}_E$. The point clouds $\boldsymbol{P}_B$ and $\boldsymbol{P}_E$ are registered to obtain the transformation matrix $\boldsymbol{Tp}_3$. Based on the previously described mathematical model for the floor-stand construction conditions, the adjustment quantities $\Delta\boldsymbol{D}$ are calculated. The segment's attitude is then precisely corrected using a 3D jack.

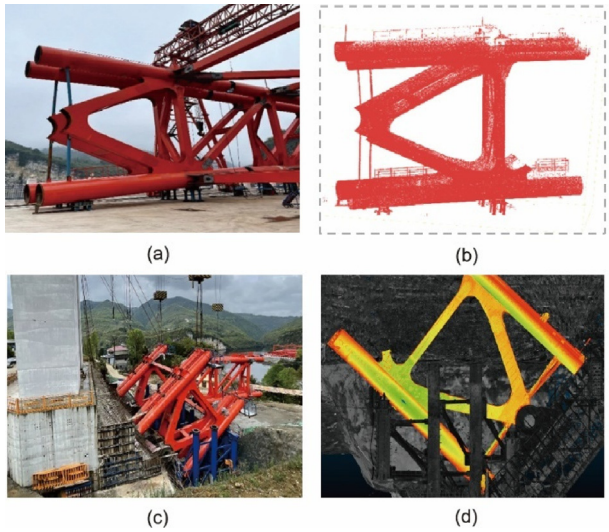

Fig. 10. Arch rib first segment: manufacturing and initial installation attitude PCD. (a) Preassembly site; (b) manufacturing attitude point cloud; (c) bridge site installation; (d) initial installation attitude point cloud.

4.3. Analysis of application effect

4.3.1. Effect analysis of cable force scheme

Incorporating the calculated cable force scheme into the model provides the arch alignment after forming, tower deviation, and

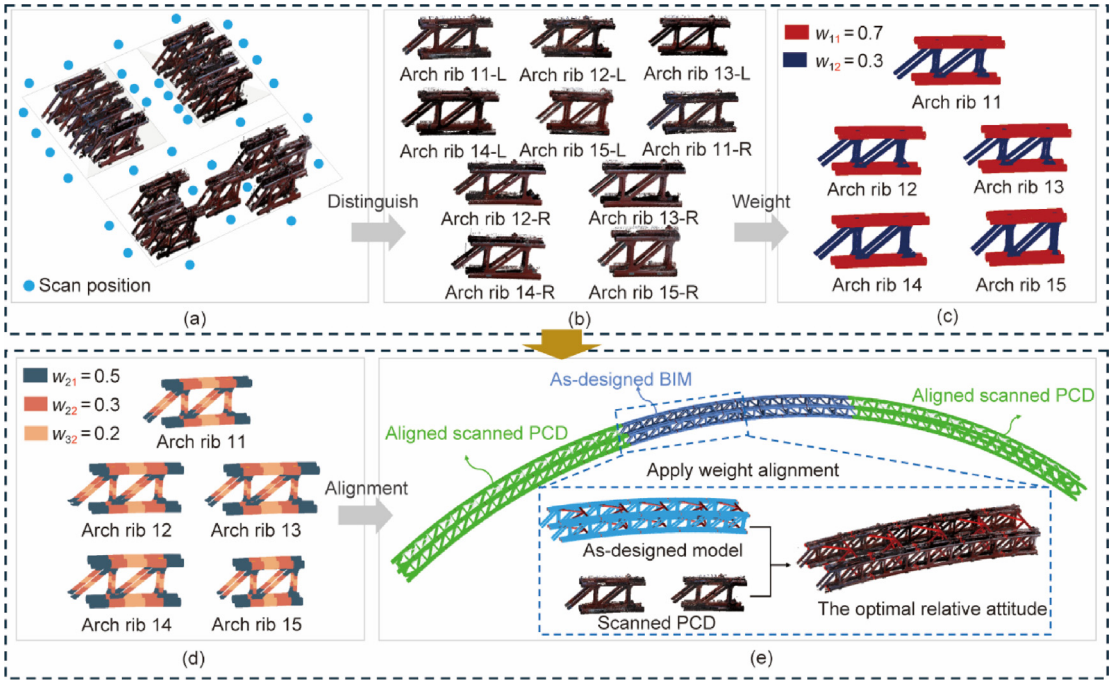

Fig. 9. Key steps for the practical application of digital assembly in the manufacturing of arch rib segments. (a) Scanning station arrangement; (b) identification and numbering of PCD; (c) assignment of semantic weights to components; (d) assignment of point cloud distribution weights; (e) digital assembly procedure.

cable force results. Fig. 11(a) compares the arch alignment after forming using the traditional zero-displacement method [12] with the method proposed in this study. The zero-displacement method (blue line) deviates from the target alignment (red line) by up to 12.67 mm, whereas the proposed method (black line) limits the maximum deviation to less than 2 mm. The traditional zero-displacement method focuses on achieving predetermined targets during construction but cannot ensure that the final arch alignment matches the design. In contrast, the proposed method establishes a mechanical state connection before and after arching, effectively controlling the arch alignment to match the target. The results demonstrate that the proposed method keeps the maximum deviation of the main arch alignment below 2 mm.

According to the *Technical Specifications for Construction of Highway Bridges and Culverts* (JTG/T 3650–2020) [44], the maximum allowable tower deviation is 1/400 of the tower height. With a steel anchor tower height of 31.79 m, the maximum deviation is 79.48 mm. As shown in Fig. 11(b), the maximum measured tower deviation is 19 mm, well within the specification, indicating effective control of tower deviation.

For the control of cable forces in the cable-stayed fastening–hanging system, both the full cross-section load-bearing state and the allowable cable force limits must be considered. Fig. 11(c) presents the distribution of cable forces on the north bank at each construction stage based on the proposed method. Within each stage, the forces of individual cables fluctuate minimally, reducing the need to partition the cable forces into multiple segments and promoting a more uniform full cross-section load-bearing behavior. Furthermore, the distribution of cable forces at each stage is reasonable, with minimal fluctuations for individual cables. The safety factor of each cable exceeds 2.5, as shown in Fig. 11(c) and Table 1, which present the distribution of cable forces and safety factors for the left tower anchor cables at each stage. The safety factor is defined as the ratio of the maximum allowable cable force to the actual cable force. According to Clause 19.4.3 of the *Technical Specifications for Construction of Highway Bridges and Culverts* (JTG/T 3650–2020) [44], the safety factor should exceed 2.0; all values in Table 1 surpass 2.5, confirming that the cable forces at each stage are reasonable.

In summary, the arch-forming optimization method proposed in this study controls the main arch rib alignment error to less than 2 mm, limits tower deviation to under 20 mm, and ensures cable forces with minimal fluctuations and safety factors above 2.5. These results demonstrate that the proposed method effectively achieves active control of both arch rib alignment and tower deviation.

4.3.2. Verifying the effectiveness of the digital manufacturing control scheme

Segments 11–15 on the south bank were connected at the assembly site using the physical assembly method to verify the effectiveness of the proposed methodology. Subsequently, the

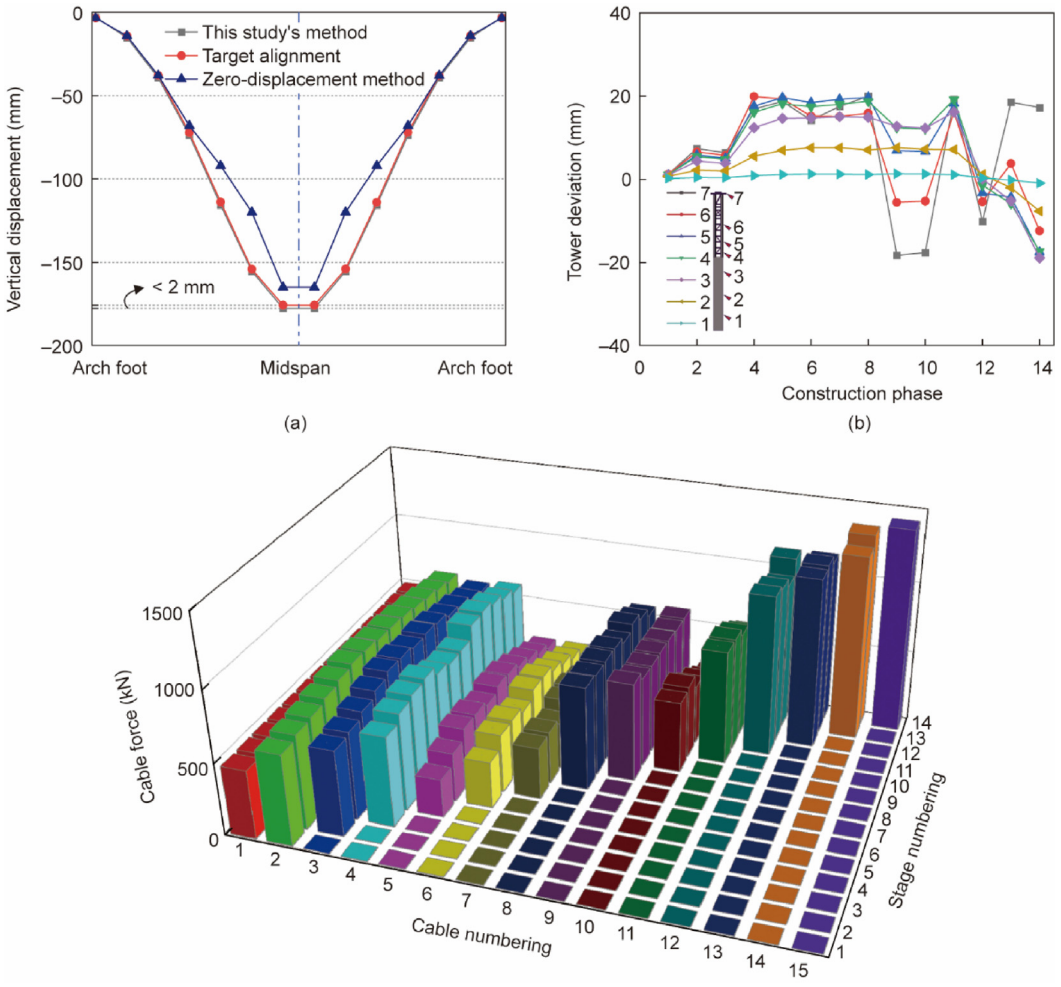

Fig. 11. Optimal cable force control results. (a) Comparison of main arch alignment; (b) tower deviation at different construction stages; (c) cable force distribution on the north bank across construction stages.

Table 1
Safety factors of the cable on the north bank at various construction stages.

Stage	Number of cables on the north bank														
	1	2	3	4	5	6	7	8	9	10	11	12	13	14	15
1	2.73	3.29	–	–	–	–	–	–	–	–	–	–	–	–	–
2	2.71	3.17	3.05	–	–	–	–	–	–	–	–	–	–	–	–
3	2.70	3.10	2.97	2.92	–	–	–	–	–	–	–	–	–	–	–
4	2.70	2.99	2.80	2.68	6.91	–	–	–	–	–	–	–	–	–	–
5	2.69	2.89	2.63	2.59	5.41	5.71	–	–	–	–	–	–	–	–	–
6	2.68	2.82	2.51	2.55	4.50	4.51	4.37	–	–	–	–	–	–	–	–
7	2.69	2.85	2.53	2.81	4.51	4.49	4.33	2.53	–	–	–	–	–	–	–
8	2.69	2.92	2.62	2.93	4.98	5.06	4.88	2.58	2.66	–	–	–	–	–	–
9	2.70	2.93	2.59	2.93	4.51	4.33	4.07	2.59	2.92	4.23	–	–	–	–	–
10	2.71	3.00	2.65	2.56	4.65	4.41	4.07	2.61	2.95	4.11	2.63	–	–	–	–
11	2.72	3.09	2.79	2.53	5.23	5.08	4.61	2.81	2.97	5.10	2.65	2.56	–	–	–
12	2.71	3.19	2.88	2.66	6.02	5.83	5.28	2.64	3.01	5.93	2.86	2.63	2.63	–	–
13	2.71	3.31	3.05	2.86	7.23	7.15	6.30	2.87	3.09	7.87	3.25	2.80	2.62	2.63	–
14	2.70	3.42	3.20	3.06	9.08	9.15	7.95	3.19	3.10	10.86	3.78	2.55	2.76	2.50	2.57

alignment of the connected arch ribs was measured. The arch ribs are numbered sequentially from left to right. The measured alignment after the connection of the arch ribs is shown in Fig. 12.

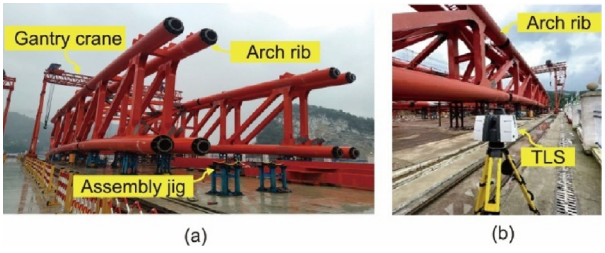

Fig. 12. Actual on-site measurement of the arch rib alignment. (a) Physical assembly; (b) scanner data acquisition.

Following the physical assembly of the structure, the elevation and axial offset values of the upper chord of the arch rib were measured by arranging designated measurement points. These measured values were then compared with the allowable limits specified in the *Specification for Manufacture and Installation of Highway Steel Bridge* (JTG/T 3651–2022) [45]. The arch rib alignment measurement points were positioned centrally along the upper chord of each arch rib, with nine measurement points evenly distributed along the arc length of each segment. The layout of the measurement point arrangement is illustrated in Fig. 13(a). After completing the physical assembly, the maximum positive elevation deviation of the upper chord arch rib was measured at 3.2 mm, and the maximum negative elevation deviation was 2.8 mm, compared with the 8 mm tolerance specified in the standard, as shown in Fig. 13(b). Similarly, the maximum positive axial deviation of the

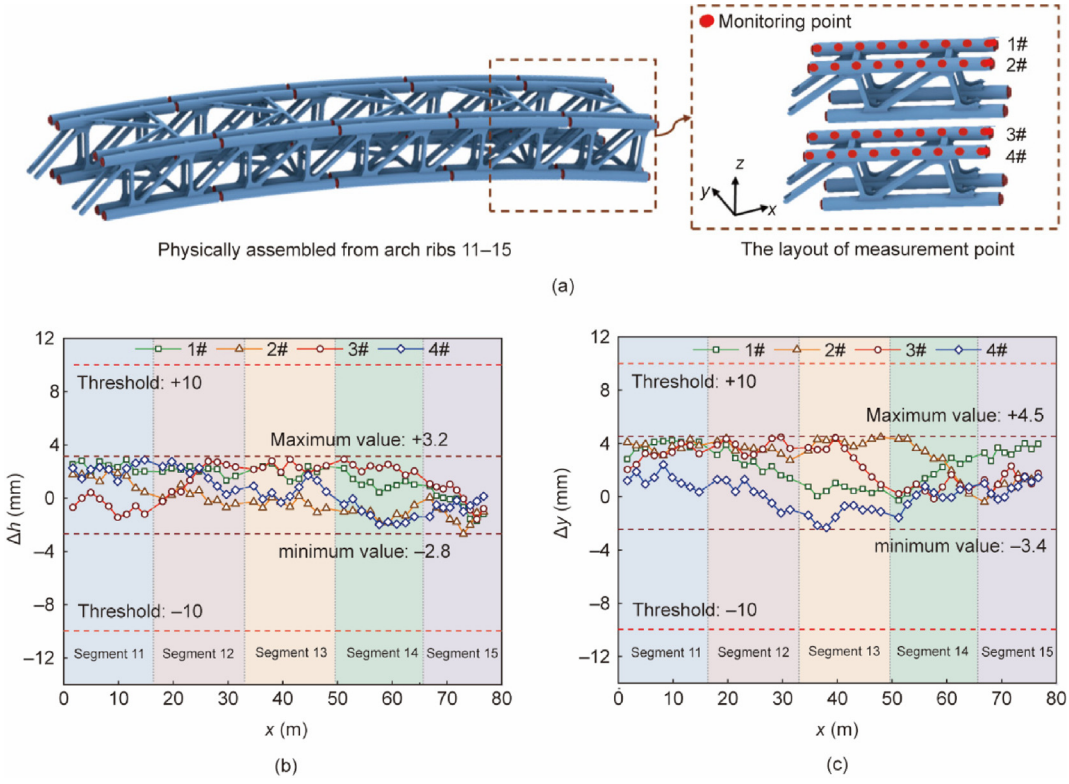

Fig. 13. Comparison of measurement data for the arch rib during physical assembly and post-installation. (a) Layout of measurement points; (b) elevation deviation values Δh of the upper chord arch ribs; (c) axial deviation values Δy of the upper chord arch ribs.

top chord arch rib reached 4.5 mm, while the maximum negative deviation was 3.4 mm, compared with the 10 mm tolerance outlined in the specification as shown in Fig. 13(c). These results demonstrate that, compared to the code limits, the alignment accuracy of the arch rib segments produced according to the extracted splicing relationship improved by 55%. Furthermore, the assembly time was reduced from 10 to 7.5 d, resulting in a 25% increase in overall manufacturing efficiency. Therefore, the digital preassembly-based manufacturing control scheme for arch ribs proposed in this study can effectively guide precise fabrication without the need for repeated physical assembly, ensuring that the manufactured arch ribs meet the accuracy requirements of the specification.

4.3.3. Result analysis of the attitude adjustment of the arch rib's first segment during installation

A 3D laser scanner was employed to capture the actual 3D attitude of the first segment of the adjusted arch rib, followed by a detailed deviation analysis against the target installation attitude. For this purpose, forty points were selected at equal intervals along the *x*-axis of each main chord. The 3D model of the first segment, along with the numbering of the main chords, is presented in Figs. 14(a) and (b). The results of the adjustment are shown in Figs. 14(c) and (d), indicating that the lateral and vertical deviations of all measurement points across the four chords remain within 2 mm. Compared with the first segment of the south bank, which was installed without employing this method, the proposed approach significantly reduces the need for repeated manual adjustments of the installation attitude, thereby shortening the adjustment period from 7 d to just 1 d and enhancing work efficiency by a factor of 6.

Currently, most long-span arch bridges utilize a construction approach similar to that of the Deyu Expressway Wujiang Bridge, in which the arch is divided into multiple prefabricated segments assembled at height using a cable-stayed fastening–hanging hoisting system. In this study, representative scenarios encompassing cable force calculation, arch rib fabrication, and arch rib installation on the Deyu Expressway Wujiang Bridge were selected to implement the proposed arch-forming method. The favorable results from these applications demonstrate that the proposed method is well-suited for large-span arch bridges employing the same segmental prefabrication and cable-stayed installation techniques as the Deyu Expressway Wujiang Bridge.

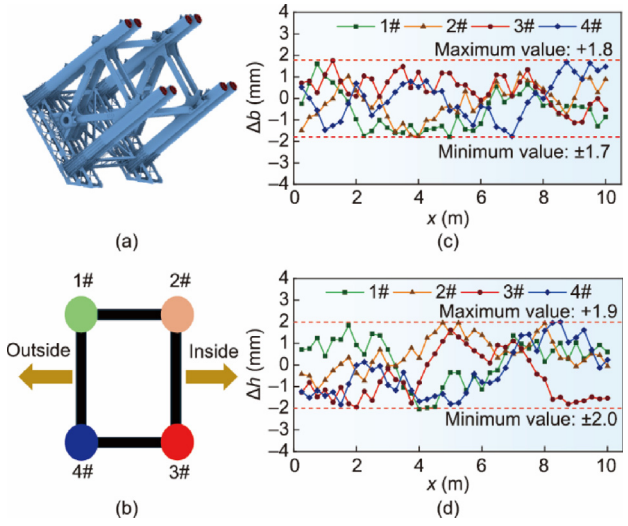

Fig. 14. Analysis of the first segment's main chord pipe numbering and installation alignment. (a) 3D model of the first segment; (b) numbering of the main chord pipes of the first segment; (c) lateral deviation analysist; (d) elevation deviation analysis.

5. Conclusions

An intelligent arch-forming method for large-span arch bridges is proposed in this study. For arch-forming calculation, a whole-process optimization model is established, through which a cable force scheme meeting the objectives throughout the construction process is computed. For manufacturing control, a method based on digital preassembly of arch ribs is presented, enabling precise fabrication of arch rib segments without the need for physical preassembly. For installation control, an automatic installation attitude adjustment strategy based on restoration to the designed shape is introduced, allowing precise one-time adjustment and positioning of the arch rib installation attitude. The proposed methodology was validated on the Deyu Expressway Wujiang Bridge, a CFST arch bridge with a main span of 504 m. Based on the results of this study, the following conclusions are drawn:

(1) A whole-process optimization model for arch-forming is established, through which an optimal cable force scheme is obtained while satisfying constraints on tower deviation, cable force, structural stress, and post-forming alignment accuracy. For the Deyu Expressway Wujiang Bridge, the deviation between the post-forming alignment and the target alignment is within 2 mm; the overall tower deviation throughout construction is within 20 mm; and the safety factor of all cables exceeds 2.5. These results demonstrate that all predefined objectives are successfully achieved.

(2) For manufacturing control, virtual preassembly of arch rib segments is performed in digital space, effectively replacing physical preassembly. This method significantly improves the overall alignment accuracy after assembly of all arch rib segments. It was applied to the manufacturing of segments 11–15 on the south bank of the Deyu Expressway Wujiang Bridge. Compared with the specification limits, the alignment accuracy of the assembled segments is improved by 55%, and the overall manufacturing efficiency of the arch ribs is increased by 25%, confirming the reliability and effectiveness of the proposed method.

(3) For installation control, accurate 3D control targets for arch rib segment installation are provided based on the original shape, accounting for environmental effects and construction loads. This allows precise one-time positioning of arch rib segments. For the first segments of the Wujiang Bridge, the measured lateral and elevation deviations were within 2 mm, and the adjustment efficiency increased sixfold. These results demonstrate that the proposed method significantly improves both the accuracy and efficiency of arch rib segment installation.

Although the proposed method is applicable to the construction of large-span arch bridges, several research areas remain for further investigation. This study primarily addresses arch bridges assembled from prefabricated steel segments. For concrete arch bridges, further research is needed to implement intelligent construction strategies effectively and to control concrete quality.

CRediT authorship contribution statement

Jianting Zhou: Writing – original draft, Funding acquisition, Conceptualization. **Yanliang Du:** Supervision, Resources, Project administration. **Yin Zhou:** Software, Project administration, Methodology. **Jinyu Zhu:** Visualization, Investigation, Formal analysis.

Declaration of competing interest

The authors declare that they have no known competing financial interests or personal relationships that could have appeared to influence the work reported in this paper.

Acknowledgments

This study was supported by the National Key R&D Program of China (2024YFB2605700), the National Natural Science Foundation of China (U24A20163), the Science and Technology Project of Sichuan Provincial Transportation Department (2023-ZL-03), the Chongqing Natural Science Foundation of China (CSTB2022TIAD-KPX0205), and the Science and Technology Project of Guizhou Provincial Transportation Department (2024-122-018).

References

[1] Zheng J, Wang J. Concrete-filled steel tube arch bridges in China. Engineering 2018;4(1):143–55.
[2] Zhang M, Zhang J, Li Y, Yu J, Zhang J, Wu L. Wind characteristics in the high-altitude difference at bridge site by wind tunnel tests. Wind Struct 2020;30(6):548–57.
[3] Zhou J, Wang S, Liu Z, Yang L, Wang Z, Li Y. Coupling dual nonlinearity of arch bridge bearing capacity analysis method. Int J Struct Stab Dyn 2023;23(16n18):2340030.
[4] Zhou J, Fan Y, Luo C, Xin J, Yang J. Design of scaled-down model test of very long rigid skeleton arch bridge. Bridge Constr 2024;54:24–30 [Chinese].
[5] Zheng J, Wang J, Mou Y, Feng Z, Han Y, Qin D. Feasibility study on design and construction of concrete filled steel tubular arch bridge with a span of 700 m. Strateg Study Chin Academy Eng 2014;16:33–7 [Chinese].
[6] Xie X, Fu Y, Deng N. Design of half-through cable-arch bridge with 700 m main span. J Southwest Jiaotong Univ 2019;54:1162–8 [Chinese].
[7] Cheng G, Liu J, Cui N, Hu H, Xu C, Tang J. Virtual trial assembly of large steel members with bolted connections based on point cloud data. Autom Constr 2023;151:104866.
[8] Jiang Y, Shu J, Ye J, Zhao W. Virtual trail assembly of prefabricated structures based on point cloud and BIM. Autom Constr 2023;155:105049.
[9] Zheng J, Du H, Mu T, Liu J, Qin D, Mei G, et al. Innovations in design, construction, and management of Pingnan Third Bridge—the largest-span arch bridge in the world. Struct Eng Int 2022;32(2):134–41.
[10] Zheng J. Recent construction technology innovations and practices for large-span arch bridges in China. Engineering 2024;41:110–29.
[11] Zhou S, Jiang L, Zeng Z, Zhou J. Simulate calculation study of cable-stayed force for arch bridge segmental construction. J Chongqing Jiaotong Univ 2000;19(3):8–12 [Chinese].
[12] Yu Y, Luo Y, Zhou W, Jiang L. Combined algorithm for the fastening stay force determinations in cantilever construction by synthesizing the zero-displacement and zero-stress state control methods. Adv Eng Sci 2024;56(3):83–9 [Chinese].
[13] Han Y, Qin D, Zheng J. Optimization calculation method for cable-stayed cantilever construction of CFST arch bridge. Highway 2018;63:100–4 [Chinese].
[14] Li Y, Wang J, Ge S. Optimum calculation method for cable force of concrete-filled steel tube arch bridge in inclined cable-stayed construction. J Highway Transp Res Dev 2017;11(1):42–8 [Chinese].
[15] Huo X, Gao L, Wu X. Study on the optimization of construction cable tensions for multi-rib butterfly-shape arch bridges. J Highway Transp Res Dev 2012;6(2):56–64 [Chinese].
[16] Qin D, Zheng J, Du H, Han Y, Zheng J, Wei L. Optimization calculation method for stayed-buckle cable force under one-time tension by fastening stay method and its application. Chin Railway Sci 2020;41:52–60 [Chinese].
[17] Zhou Q, Zhou JT, Ma H, Li XG, Zhang L. Improved algorithm of cable force for one-time cable tensioning on steel tube arch ribs with segmental hoisting. J Traffic Transp Eng 2020;20(1):92–101 [Chinese].
[18] Zhang JL, Hellmich C, Mang HA, Yuan Y, Pichler B. Application of transfer relations to structural analysis of arch bridges. Comput Methods Eng Sci 2018;24:199–215.
[19] Tian Z, Zhang Z, Ning C, Peng T, Guo Y, Cao Z. Multi-objective optimization of cable force of arch bridge constructed by cable-stayed cantilever cast-*in-situ* method based on improved NSGA-II. Structures 2024;59:105782.
[20] Duan J, Wang H, Hao T. Optimal model of arch bridge cable force based on improved grey wolf algorithm and support vector machine. Comput Eng Des 2023;44:457–65.
[21] Case F, Beinat A, Crosilla F, Alba IM. Virtual trial assembly of a complex steel structure by generalized Procrustes analysis techniques. Autom Constr 2014;37:155–65.
[22] Maset E, Scalera L, Zonta D, Alba IM, Crosilla F, Fusiello A. Procrustes analysis for the virtual trial assembly of large-size elements. Robot Comput-Integr Manuf 2020;62:101885.
[23] Tamai S, Yagata Y, Hosoya T. New technologies in fabrication of steel bridges in Japan. J Construct Steel Res 2002;58(1):151–92.
[24] Wang YG, He XJ, He J, Fan C. Virtual trial assembly of steel structure based on BIM platform. Autom Constr 2022;141:104395.
[25] Paneru S, Jeelani I. Computer vision applications in construction: current state, opportunities & challenges. Autom Constr 2021;132:103940.
[26] Jin Y, Yu L, Li G, Fei S. A 6-DOFs event-based camera relocalization system by CNN-LSTM and image denoising. Expert Syst Appl 2021;170:114535.
[27] Tang Y, Huang B, Wang S, Zhou J, Xiang Z, Sheng C, et al. Computer vision-based real-time continuous monitoring of the pose for large-span bridge cable lifting structures. Autom Constr 2024;162:105383.
[28] Guan ZX, Yi TH, Yang DH, Li HN. Dynamic calibrating of multiscale bridge model using long-term stochastic vehicle-induced responses. J Bridg Eng 2024;29(9):04024066.
[29] Wang Z, Yi TH, Yang DH, Li HN, Liu H. Early warning of abnormal bridge frequencies based on a local correlation model under multiple environmental conditions. J Bridg Eng 2023;28(2):04022139.
[30] Huang HB, Yi TH, Li HN, Liu H. Sparse Bayesian identification of temperature-displacement model for performance assessment and early warning of bridge bearings. J Struct Eng 2022;148(6):04022052.
[31] Bosché F, Ahmed M, Turkan Y, Haas CT, Haas R. The value of integrating scan-to-BIM and scan-vs-BIM techniques for construction monitoring using laser scanning and BIM: the case of cylindrical MEP components. Autom Constr 2015;49:201–13.
[32] Hu G, Zhou Y, Xiang Z, Zhao L, Chen G, Li T, et al. Fast and accurate generation method of geometric digital twin model of RC bridge with box chambers based on terrestrial laser scanning. Remote Sens 2023;15(18):4440.
[33] Rausch C, Nahangi M, Perreault M, Haas CT, West J. Optimum assembly planning for modular construction components. J Comput Civ Eng 2017;31(1):04016039.
[34] Kim MK, Wang Q, Park JW, Cheng JCP, Sohn H, Chang CC. Automated dimensional quality assurance of full-scale precast concrete elements using laser scanning and BIM. Autom Constr 2016;72:102–14.
[35] Xu Y, Luo Y, Zhang J. Laser-scan based pose monitoring for guiding erection of precast concrete bridge piers. Autom Constr 2022;140:104347.
[36] Qin S. Control method of stress-free status for erection of cable-stayed bridges. Bridge Constr 2003;2:31–4. Chinese.
[37] Trentini EVW, Parsekian GA, Bittencourt TN. Multiobjective optimization of bridge and viaduct design: comparative study of metaheuristics and parameter calibration. Eng Struct 2024;312:118252.
[38] Xiao R, Guo W. Influence matrices method for structural adjustment calculation of internal forces and displacements of concern sections. Chin J Comput Mech 1992;1:91–9 [Chinese].
[39] Deb K, Pratap A, Agarwal S, Meyarivan T. A fast and elitist multiobjective genetic algorithm: NSGA-II. IEEE Trans Evol Comput 2002;6(2):182–97.
[40] Bueno M, Bosché F, González-Jorge H, Martínez-Sánchez J, Arias P. 4-plane congruent sets for automatic registration of as-is 3D point clouds with 3D BIM models. Autom Constr 2018;89:120–34.
[41] Cai Z, Chin TJ, Bustos AP, Schindler K. Practical optimal registration of terrestrial LiDAR scan pairs. ISPRS J Photogramm Remote Sens 2019;147:118–31.
[42] Dong Z, Yang B, Liang F, Huang R, Scherer S. Hierarchical registration of unordered TLS point clouds based on binary shape context descriptor. ISPRS J Photogramm Remote Sens 2018;144:61–79.
[43] Besl PJ, McKay ND. A method for registration of 3-D shapes. IEEE Trans Pattern Anal Mach Intell 1992;14(2):239–1235.
[44] Ministry of Transport of the People's Republic of China. JTG/T 3650–2020: Technical Specifications for Construction of Highway Bridges and Culverts. Chinese Standard. Beijing: Ministry of Transport of the People's Republic of China; 2020. [Chinese].
[45] Ministry of Transport of the People's Republic of China. JTG/T 3651–2022: Specification for Manufacture and Installation of Highway Steel Bridge. Chinese Standard. Beijing: Ministry of Transport of the People's Republic of China; 2022. [Chinese].